The Astrophysical Journal Letters, 990:L68 (18pp), 2025 September 10 https://doi.org/10.3847/2041-8213/adfe52

Early Shock Cooling Observations and Progenitor Constraints of Type IIb Supernova SN 2024uwq

Bhagya M. Subrayan[1], David J. Sand[1], K. Azalee Bostroem[1,13], Saurabh W. Jha[2], Aravind P. Ravi[3], Michaela Schwab[2], Jennifer E. Andrews[4], Griffin Hosseinzadeh[5], Stefano Valenti[3], Yize Dong (董一泽)[3], Jeniveve Pearson[1], Manisha Shrestha[1], Lindsey A. Kwok[6], Emily Hoang[3], Jeonghee Rho[7], Seong Hyun Park[8], Sung-Chul Yoon[8], T. R. Geballe[4], Joshua Haislip[9], Daryl Janzen[10], Vladimir Kouprianov[9], Darshana Mehta[3], Nicolás Meza Retamal[3], Daniel E. Reichart[9], Moira Andrews[11,12], Joseph Farah[11,12], Megan Newsome[11,12], D. Andrew Howell[11,12], and Curtis McCully[11]

[1] Steward Observatory, University of Arizona, 933 North Cherry Avenue, Tucson, AZ 85721-0065, USA; bsubrayan@arizona.edu
[2] Department of Physics and Astronomy, Rutgers, the State University of New Jersey, 136 Frelinghuysen Road, Piscataway, NJ 08854-8019, USA
[3] Department of Physics and Astronomy, University of California, Davis, 1 Shields Avenue, Davis, CA 95616-5270, USA
[4] Gemini Observatory, 670 North A'ohoku Place, Hilo, HI 96720-2700, USA
[5] Department of Astronomy & Astrophysics, University of California, San Diego, 9500 Gilman Drive, MC 0424, La Jolla, CA 92093-0424, USA
[6] Center for Interdisciplinary Exploration and Research in Astrophysics (CIERA), Northwestern University, Evanston, IL 60208, USA
[7] SETI Institute, 339 Bernardo Avenue, Suite 200, Mountain View, CA 94043, USA
[8] Department of Physics and Astronomy, Seoul National University, Gwanak-ro 1, Gwanak-gu, Seoul, 08826, Republic of Korea
[9] Department of Physics and Astronomy, University of North Carolina, 120 East Cameron Avenue, Chapel Hill, NC 27599, USA
[10] Department of Physics & Engineering Physics, University of Saskatchewan, 116 Science Place, Saskatoon, SK S7N 5E2, Canada
[11] Las Cumbres Observatory, 6740 Cortona Drive, Suite 102, Goleta, CA 93117-5575, USA
[12] Department of Physics, University of California, Santa Barbara, CA 93106-9530, USA
Received 2025 May 1; revised 2025 August 12; accepted 2025 August 13; published 2025 September 10

Abstract

We present early multiwavelength photometric and spectroscopic observations of the Type IIb supernova SN 2024uwq, capturing its shock-cooling emission phase and double-peaked light-curve evolution. Early spectra reveal broad H (v 15,500 km s^{-1}) and He I P Cygni profiles of similar strengths. Over time the He I lines increase in strength while the H decreases, consistent with a hydrogen envelope ($M_{\rm env} = 0.7$–$1.35\,M_{\odot}$) overlying helium-rich ejecta. Analytic modeling of early shock cooling emission and bolometric light analysis constrains the progenitor to a partially stripped star with radius $R = 10$–$60\,R_{\odot}$, consistent with a blue/yellow supergiant with an initial zero-age main-sequence mass of 12–20 $M_{\odot}$ likely stripped via binary interaction. SN 2024uwq occupies a transitional position between compact and extended Type IIb supernovae, highlighting the role of binary mass transfer efficiency in shaping a continuum of stripped-envelope progenitors. Our results underscore the importance of early UV/optical observations to characterize shock breakout signatures critical to map the diversity in evolutionary pathways of massive stars. Upcoming time-domain surveys, including Rubin Observatory's LSST and UV missions like ULTRASAT and UVEX, will revolutionize our ability to systematically capture these early signatures, probing the full diversity of stripped progenitors and their explosive endpoints.

Unified Astronomy Thesaurus concepts: Core-collapse supernovae (304); Supernovae (1668); Binary stars (154); Stellar evolution (1599)

Materials only available in the online version of record: data behind figure

1. Introduction

Massive stars ($\gtrsim 8\,M_{\odot}$) explode as core-collapse supernovae (CCSNe). While the majority of CCSNe show hydrogen in their spectra, a subset undergoes extensive mass loss, shedding their outer H and He layers to become stripped-envelope supernovae (SESNe; S. E. Woosley et al. 1994; A. V. Filippenko 1997; A. Gal-Yam 2017). Among CCSNe, Type IIb supernovae (SNe IIb) are transitional objects—while their early spectra have weak hydrogen lines, these lines fade within weeks, revealing helium-dominated profiles similar to those of SNe Ib that are hydrogen-poor explosions marked by strong helium lines in their optical spectra (e.g., SN 1987K, A. V. Filippenko 1988; SN 1993J, A. V. Filippenko et al. 1993; M. W. Richmond et al. 1994; SN 2008ax, A. Pastorello et al. 2008; SN 2011dh, I. Arcavi et al. 2011; A. M. Soderberg et al. 2012; SN 2011ei, D. Milisavljevic et al. 2013; SN 2011fu, A. Morales-Garoffolo et al. 2015; SN 2013df, S. D. Van Dyk et al. 2014; A. Morales-Garoffolo et al. 2014; SN 2016gkg, I. Arcavi et al. 2017; L. Tartaglia et al. 2017; M. C. Bersten et al. 2018). This spectral evolution indicates that the progenitors retain only a thin hydrogen envelope ($\lesssim 1\,M_{\odot}$) at explosion, offering a unique window into the final stages of massive-star evolution (M. W. Richmond et al. 1994; T. Matheson et al. 2000). Although it critically shapes the final structure of the progenitor, this extensive mass loss driven by mechanisms such as stellar winds (S. E. Woosley et al. 1993; C. Georgy et al. 2013; J. H. Groh et al. 2013b), binary interactions (P. Podsiadlowski 2008; N. Smith 2014; R. Ouchi & K. Maeda 2017; N. Soker 2017), or rotational stripping (J. Groh et al. 2013a)

[13] LSSTC Catalyst Fellow.

remains poorly understood. Observational studies reveal a diverse progenitor population, including yellow supergiants (YSGs; e.g., SN 2011dh), K supergiants (e.g., SN 1993J) and Wolf–Rayet stars (e.g., SN 2008ax), spanning initial masses of 10–28 $M_{\odot}$ (A. V. Filippenko et al. 1993; R. M. Crockett et al. 2008; I. Arcavi et al. 2011). Probing circumstellar material from the radio/X-ray counterparts of these SNe has also provided constraints on the wind velocities and mass-loss history responsible for the stripping of the outer envelope. Such diversity underscores the complex interplay of binary evolution and stellar physics in shaping pre-SN systems (N. Sravan et al. 2020).

A characteristic of many SNe IIb is their double-peaked light curve. The brief initial peak, lasting hours to days, arises from shock cooling emission (SCE) as the explosion's thermalized energy radiates from the extended envelope of the progenitor (M. W. Richmond et al. 1994; I. Arcavi et al. 2017; K. K. Das et al. 2023). Analytical and numerical models (I. Rabinak & E. Waxman 2011; A. L. Piro 2015; A. L. Piro et al. 2021) link the cooling phase with the density and radius of the envelope, with recent extensions incorporating multizone dynamics and UV line blanketing (N. Sapir & E. Waxman 2017; J. Morag et al. 2023). These models, when applied to high-cadence observations of nearby SNe IIb that resolve the SCE phase (M. W. Richmond et al. 1994; I. Arcavi et al. 2017; P. Armstrong et al. 2021; J. R. Farah et al. 2025), suggest progenitors with extended envelopes (100–500 $R_{\odot}$) and low residual hydrogen masses (0.01–1 $M_{\odot}$), consistent with pre-explosion imaging of YSGs and red supergiants (RSGs; L. Tartaglia et al. 2017; M. C. Bersten et al. 2018; C. D. Kilpatrick et al. 2022).

In this Letter, we present a comprehensive analysis of SN 2024uwq, a nearby (D 47 Mpc) SN IIb with early multiwavelength photometric and spectroscopic observations. In Section 2, we detail the discovery, distance estimation, and reddening considerations for SN 2024uwq. Section 3 describes our observations and data reduction procedures, which include both imaging and optical spectroscopy. In Section 4, we analyze the photometric data, focusing on the early SCE, color evolution, bolometric luminosity, and estimates of the synthesized ^{56}Ni mass. Section 5 presents the spectroscopic features and their temporal evolution, comparing them with other SNe IIb. We present early SCE modeling to constrain progenitor properties for various analytical frameworks in Section 6. In Section 7, we report our results and findings on SN 2024uwq, situating it within the broader context of SESNe and discussing its implications for progenitor scenarios. Section 8 then summarizes our conclusions and outlines the prospects for early, high-cadence follow-up observations with upcoming missions such as ULTRASAT, UVEX, and LSST.

2. Discovery, Distance, and Reddening

SN 2024uwq was discovered by the Asteroid Terrestrial-impact Last Alert System (ATLAS; J. L. Tonry et al. 2018; K. W. Smith et al. 2020) on 2024 September 07 02:33:57.02 UT (MJD = 60560.11) with a discovery magnitude of o = 17.38 mag (J. Tonry et al. 2024). All dates and times used in this work are reported in the Coordinated Universal Time (UTC) standard. SN 2024uwq is located in NGC 6902 (Figure 1) at J2000 coordinates = $20^{h}24^{m}36\overset{s}{.}770$ and = −43°40 10. 13. SN 2024uwq is situated at a relatively remote location from the center of its host galaxy; see Figure 1. SNe IIb are generally associated with active star-forming

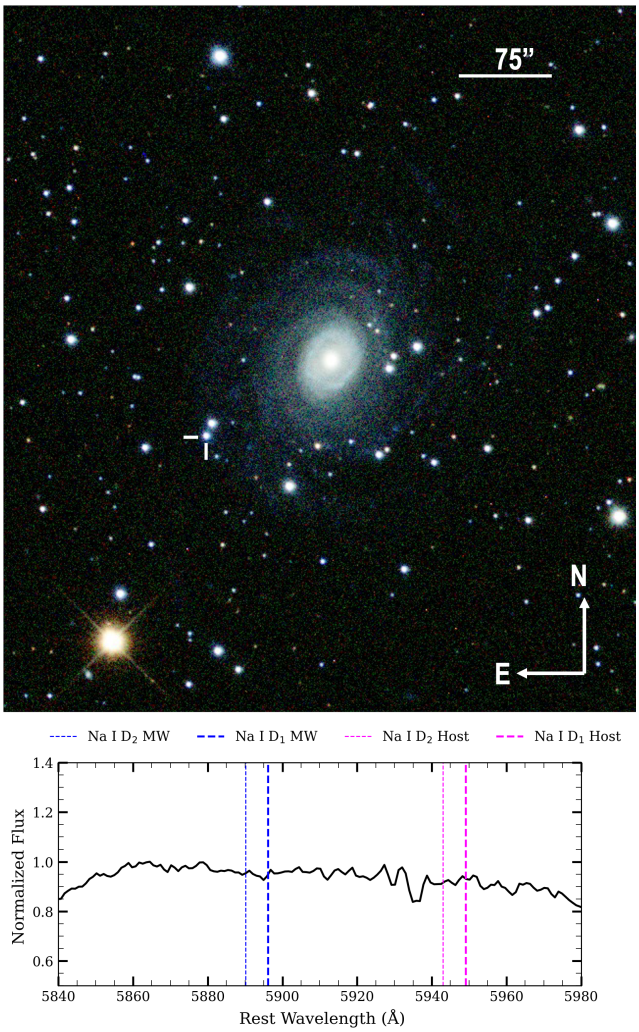

Figure 1. Top: composite *gri* image of SN 2024uwq obtained using Las Cumbres Observatory observations on 2024 September 28. SN 2024uwq is marked with white cross hairs in the composite image. Bottom: normalized spectrum of SN 2024uwq showing Na I D absorption from the MW (blue) and host galaxy (pink), used to estimate line-of-sight extinction.

regions within galactic disks but can also be located at large offsets from their host (A. A. Hakobyan et al. 2009; P. L. Kelly & R. P. Kirshner 2012). With a projected offset of 110 (20 kpc), SN 2024uwq resides relatively far from the center of the host galaxy, but within its farthest spiral arms.[14] The last available nondetection was reported by ATLAS on 2024 September 04 at 03:51:10 (MJD = 60557.16), 3 days prior to the discovery date, with a 3σ limiting magnitude of o = 19.3 mag. Throughout this Letter, we adopt the explosion date (t_0) as the midpoint between the last ATLAS nondetection and the discovery date, which is at MJD = 60558.63 1.5, where the uncertainty covers the time between nondetection and discovery. Unless stated otherwise, all phases reported in this work are calculated using this explosion date.

SN 2024uwq was initially classified as an SN Ic-BL by the extended Public European Southern Observatory (ESO) Spectroscopic Survey of Transient Objects (ePESSTO+: S. J. Smartt 2015) at a redshift z = 0.009 (M. Ramirez et al. 2024). On 2024 September 17, SN 2024uwq was

[14] https://www.legacysurvey.org/

reclassified as an SN IIb using a spectrum taken by the Global Supernova Project (GSP; A. Howell (2024)). This classification, based on GELATO (A. H. Harutyunyan et al. 2008) and Supernova Identification (SNID; S. Blondin & J. L. Tonry 2011) code comparisons, shows that the spectrum best matches young SN IIb templates with redshifts between 0.003 and 0.009 (K. A. Bostroem 2024). We adopted a redshift of $z = 0.009$ in this work, as this value aligns closely with SN templates and is confirmed by the Na I D absorption features detected in our highest signal-to-noise ratio (SNR) spectra. We use the Tully–Fisher (R. B. Tully et al. 2009) distance modulus value of $\mu = 33.34$ 0.40 mag, which yields a distance of $D = 46.6$ 8.6 Mpc, which is adopted throughout this Letter.

To estimate reddening along the line of sight to SN 2024uwq, we considered contributions from both the Milky Way (MW) and the host galaxy. Using the high-SNR Southern African Large Telescope (SALT) spectrum (R 600–2000) obtained on 2024 October 17, we measured the equivalent widths (EWs) of Na I D absorption lines, which are empirically correlated with reddening owing to their association with interstellar gas and dust (D. Poznanski et al. 2012). We continuum-normalized the observed spectrum and modeled the blended Na I D_2 and Na I D_1 absorption lines from MW with a single Gaussian profile. This yielded a total EW of 0.32 0.04 Å. Using the relationship between EW and reddening as given in D. Poznanski et al. (2012), we derived an MW reddening of $E(B-V)_{\rm MW} = 0.034$ 0.025 mag. We compared our above reddening estimate with the dust maps of E. F. Schlafly & D. P. Finkbeiner (2011), which give $E(B-V)_{\rm MW} = 0.034$ 0.001 mag for the direction of SN 2024uwq. This value is consistent with our Na I D–based measurement.

For the host galaxy, we inspected the observed spectrum for Na I D absorption features at observed wavelengths D_2 (λ5949) and D_1 (λ5943) corresponding to the rest-frame D_2 (λ5890) and D_1 (λ5896) lines (see Figure 1). No significant absorption dips were detected, and we set an upper limit on the host galaxy EW of Na I D to <0.03 Å by measuring a 3σ noise level in the continuum. This corresponds to a reddening of $E(B-V)_{\rm host} < 0.02$ mag. Given that this upper limit is comparable to the uncertainty in $E(B-V)_{\rm MW}$, we assume that the host galaxy's contribution to reddening is negligible. Therefore, we adopt the total reddening value $E(B-V)_{\rm MW}$ 0.034 0.001 mag and apply the extinction law of J. A. Cardelli et al. (1989) with $R_V = 3.1$. Table 1 summarizes the relevant physical quantities for SN 2024uwq.

Table 1
Properties of SN 2024uwq

Parameter	Value
R.A. (J2000)	20:24:36.76
Decl. (J2000)	−43:40:09.9
Last nondetection (MJD)	60557.16
First detection (MJD)	60560.10
Explosion epoch (MJD)[a]	60558.63 1.5
Redshift (z)[b]	0.009
Distance modulus [c]	33.34 0.40 mag
Distance[c]	46.6 8.6 Mpc
$E(B-V)_{\rm MW}$[d]	0.034 0.025 mag
$E(B-V)_{\rm host}$[d]	<0.02 mag
$E(B-V)_{\rm MW}$[e]	0.034 0.001 mag
Peak magnitude ($V_{\rm max}$)	−17.79 0.4 mag

Notes.
[a] Midpoint of last nondetection and first detection.
[b] From best match SNID templates.
[c] Estimates from R. B. Tully et al. (2009).
[d] From the Na I D absorption lines.
[e] From E. F. Schlafly & D. P. Finkbeiner (2011) MW dust maps.

3. Observations and Data Reduction

3.1. Imaging

An extensive photometric campaign was launched immediately after the discovery of SN 2024uwq to ensure comprehensive coverage of its early light-curve evolution. High-cadence observations of SN 2024uwq were performed in *U, B, V, g, r,* and *i* bands using the worldwide network of 0.4 and 1 m telescopes available through the Las Cumbres Observatory (T. M. Brown et al. 2013) with the Global Supernova Project. Data were processed with the PyRAF-based pipeline `lcogtsnpipe` (S. Valenti et al. 2016) using point-spread function (PSF) fitting. The *UBV* magnitudes were calibrated in the Vega system against standard fields observed with the same telescope on the same night, using the Landolt catalog (A. U. Landolt 1992). For the *gri* bands, calibrations were performed in the AB magnitude system using reference stars from the American Association of Variable Star Observers (AAVSO) Photometric All-Sky Survey (APASS; A. A. Henden et al. 2009). We perform direct PSF photometry on the images, assuming low host galaxy contamination due to the SN's spatial offset from NGC 6902.

Additional early high-cadence photometry of SN 2024uwq was obtained as part of the Distance Less Than 40 Mpc (DLT40) survey (L. Tartaglia et al. 2018) using the PROMPT-MO 0.4 m telescope at Meckering Observatory in Australia, through the Skynet Robotic Telescope Network (D. Reichart et al. 2005). Observations were conducted in *B, V, g, r,* and *i* bands, as well as in a filterless "Open" wide-band mode. The wide-band data were calibrated to the Sloan Digital Sky Survey *r* band following the reduction procedures detailed in L. Tartaglia et al. (2018), while the multiband aperture photometry, performed with `photutils` (L. Bradley et al. 2022), was calibrated using the APASS catalog.

All publicly available ATLAS photometry of SN 2024uwq observed in *c* and *o* bands was retrieved using the ATLAS forced photometry service (J. L. Tonry et al. 2018; K. W. Smith et al. 2020).[15]

High-cadence UV and optical observations of SN 2024uwq were also obtained with the Ultraviolet/Optical Telescope (UVOT; P. W. A. Roming et al. 2005) on board the Neil Gehrels Swift Observatory (N. Gehrels et al. 2004). The data, retrieved from the NASA Swift Data Archive,[16] were processed using standard tools provided within the HEASoft[17] package. Photometry was performed in the *uvw1*, *uvm2*, *uvw2*, U_S, B_S, and V_S bands. A source aperture of 3 was used, centered on the SN position, with background subtraction performed from nearby regions free of contaminating sources. Although no pre-explosion template images were available, host galaxy contamination was assumed to be negligible and therefore

[15] https://fallingstar-data.com/forcedphot/
[16] https://heasarc.gsfc.nasa.gov/cgi-bin/W3Browse/swift.pl
[17] https://heasarc.gsfc.nasa.gov/docs/software/heasoft/

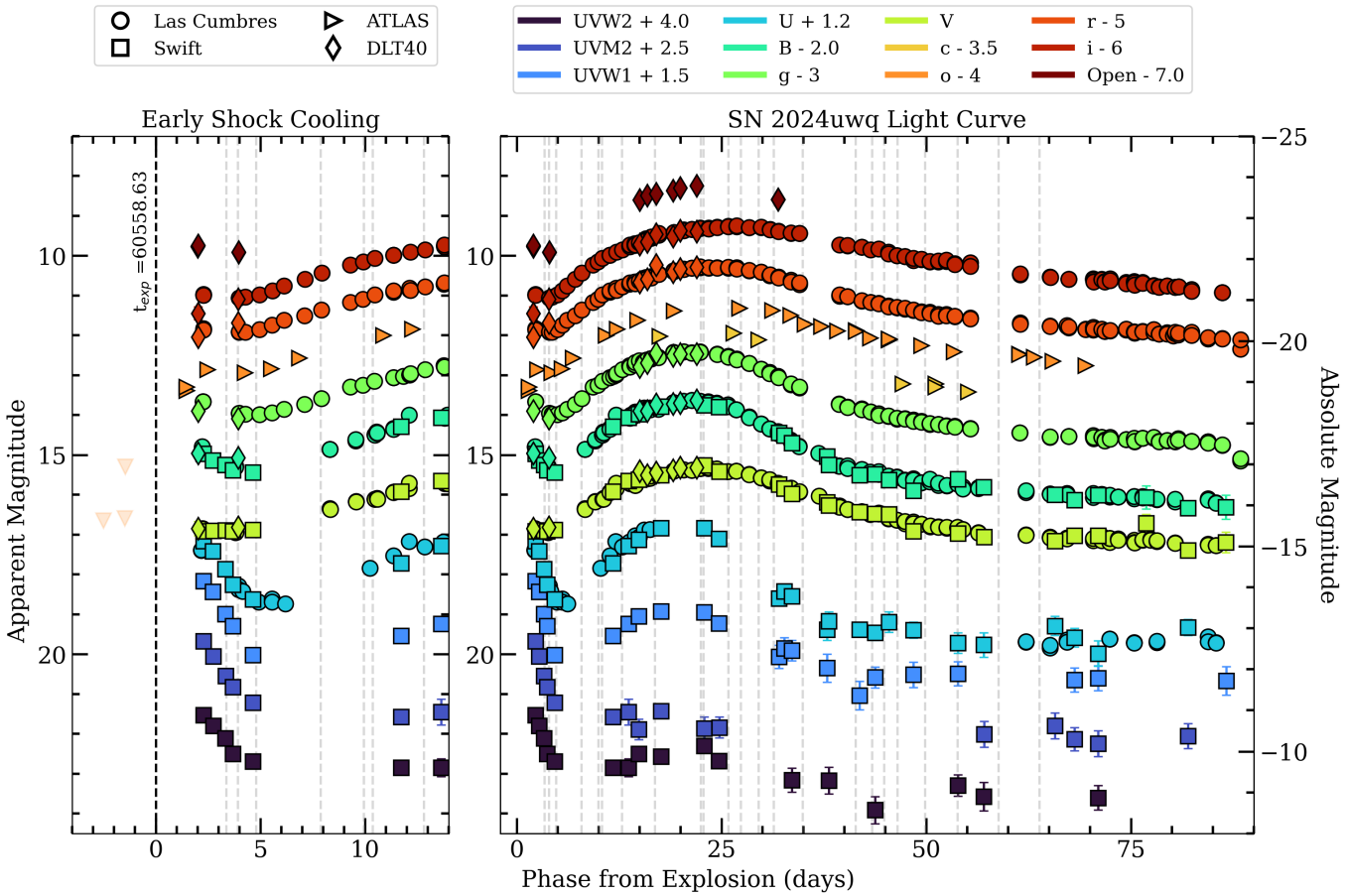

Figure 2. Multiwavelength observations of SN 2024uwq with early phases of the light curve showing characteristic SCE from the progenitor. The offsets for each bands are marked in the legend. The time of explosion is marked in the left panel, which zooms in on the early light-curve evolution. The observations provided in this figure are not corrected for extinction. The gray vertical lines mark the phases where optical spectra were obtained. The photometric data used to generate this figure are available as data behind the figure.

(The data used to create this figure are available in the online article.)

not subtracted. The zero-points for photometric calibration were adopted from A. A. Breeveld et al. (2010), incorporating time-dependent sensitivity corrections updated in 2020. All light curves derived from imaging observations are presented in Figure 2.

3.2. Spectroscopy

A series of early high-cadence spectroscopic observations of SN 2024uwq was carried out using multiple facilities. Low-resolution optical spectra were acquired with the FLOYDS spectrograph mounted on the 2.0 m Faulkes Telescope South (FTS) at Siding Spring Observatory, Australia, through the Las Cumbres Observatory as part of the Global Supernova Project collaboration. Observations were performed with a 2 -wide slit aligned at the parallactic angle. One-dimensional spectra were extracted, reduced, and calibrated according to standard procedures using the FLOYDS reduction pipeline (S. Valenti et al. 2014).

Spectroscopic observations of SN 2024uwq were also acquired using the Robert Stobie Spectrograph (RSS) on SALT (K. W. Smith et al. 2006). Data were reduced with a custom pipeline built in the PySALT package (S. M. Crawford et al. 2010), incorporating standard processing steps such as bias subtraction, flat-fielding, wavelength calibration using arc lamp exposures, and flux calibration with standard spectrophotometric stars. Additional optical spectra were also obtained with the Goodman High-Throughput Spectrograph (HTS) on the 4.1 m Southern Astrophysical Research Telescope (SOAR) for three epochs. Data reduction was performed using the Goodman HTS[18] pipeline, employing standard reduction procedures.

Near-IR (NIR) spectroscopy of SN 2024uwq was obtained using the Flamingos-2 instrument mounted on the Gemini-South telescope (S. S. Eikenberry et al. 2004; S. Eikenberry et al. 2012), as part of program GS-2024B-Q-215. The NIR observations were conducted on 2024 November 18 for the HK spectra (with an exposure time of 18 × 120 s at a relatively high air mass of 1.7) and on 2024 November 23 for the JH spectra (with an exposure time of 8 × 120 s). The data were reduced using custom IRAF scripts. Compared to GNIRS spectra from the Gemini-North telescope (e.g., J. Rho et al. 2018), Flamingos-2 spectra are less sensitive.

4. Photometry and Light-curve Evolution

4.1. Light Curve with Early Shock Cooling Emission

The multiwavelength light curve of SN 2024uwq, presented in Figure 2, reveals a distinct early-time emission excess followed by a rapid decline and a subsequent, more luminous

[18] https://soardocs.readthedocs.io/projects/goodman-pipeline/en/latest/

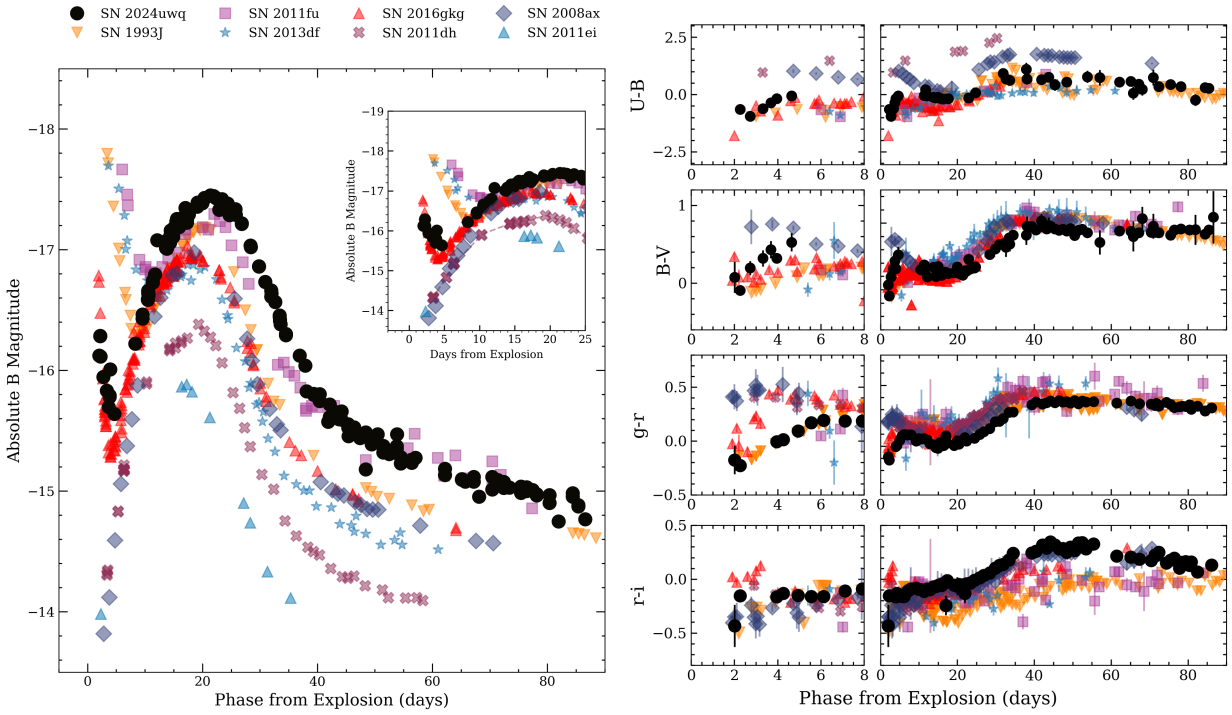

Figure 3. Left: absolute B-band light curve of SN 2024uwq in comparison with SNe IIb in the literature, with a zoom-in on the earliest phases shown in the inset. Right: extinction-corrected $U-B$, $B-V$, $g-r$, and $r-i$ color evolution of SN 2024uwq in comparison to the color evolution of typical SNe IIb. We use the relationships prescribed in K. Jordi et al. (2006) for converting $V-R$, $R-I$ to $g-r$, $r-i$, respectively (for SN 1993J, SN 2011dh, SN 2011ei, SN 2011fu, and SN 2013df). Data used in this figure are from M. W. Richmond et al. (1994; SN 1993J), A. Pastorello et al. (2008; SN 2008ax), I. Arcavi et al. (2011; SN 2011dh), A. Morales-Garoffolo et al. (2015; SN 2011fu), A. Morales-Garoffolo et al. (2014; SN 2013df), and L. Tartaglia et al. (2017) and C. D. Kilpatrick et al. (2022; SN 2016gkg).

second peak. The initial rise is poorly constrained, with only the initial ATLAS o-band data clearly showing a rise between the first and second epoch of observations. The light curve then declines rapidly within the next 3 days, after which the optical magnitudes brighten again toward the second maximum. In the Swift bands, after the initial decline, the rise to the second peak is less pronounced, with the *UVM2* and *UVW2* bands showing a flattening trend after the initial excess. We measure an absolute magnitude of $M_B = -16.3$ mag for the first observation in the B band, which occurred approximately 2 days after the explosion. This is followed by a decline to $M_B = -15.7$ mag within 1.5 days of the initial peak. After +5 days, the light curve brightens again, reaching a more luminous secondary peak with an absolute magnitude of $M_B = -17.5$ mag around +20 days from the explosion epoch.

We compare the absolute B-band light curve of SN 2024uwq with other well-studied SNe IIb, including SN 1993J (M. W. Richmond et al. 1994), SN 2008ax (A. Pastorello et al. 2008), SN 2011ei (D. Milisavljevic et al. 2013), SN 2011dh (I. Arcavi et al. 2011), SN 2011fu (A. Morales-Garoffolo et al. 2015), SN 2013df (A. Morales-Garoffolo et al. 2014), and SN 2016gkg (L. Tartaglia et al. 2017), as shown in Figure 3. SN 2024uwq's early light curve shares close similarities with those of SN 1993J, SN 2011fu, SN 2013df, and SN 2016gkg, all of which exhibit characteristic early-time SCE. This early emission suggests an explosion originating from an extended progenitor star, contrasting with SNe like SN 2008ax, SN 2011ei, and SN 2011dh, which shows either a weak or absent early excess due to their more compact progenitors (R. A. Chevalier & A. M. Soderberg 2010). Although SN 2016gkg exhibits the most similar overall shape of the early light curve to SN 2024uwq in terms of decline and rise timescales, there are notable differences in the early excess and second peak luminosities. The initial emission excess observed in SN 2016gkg is significantly more luminous than SN 2024uwq at comparable early epochs (L. Tartaglia et al. 2017; C. D. Kilpatrick et al. 2022). In contrast, as shown in Figure 3, the second peak of SN 2024uwq reaches a higher luminosity than that of SN 2016gkg. When comparing SN 2024uwq, it is crucial to acknowledge that despite the earliest ATLAS observations, its true early excess peak remains uncertain owing to observational cadence and the likelihood of band-dependent differences in the early emission.

We measure the B-band apparent magnitude decline rate for SN 2024uwq after the initial maximum to be 0.64 mag day^{-1} over the first 5 days. This decline is slower than that of SN 2016gkg, which showed a steeper decline of 0.81 mag day^{-1} over 2 days, but faster than SN 1993J's more gradual decline of 0.31 mag day^{-1} over 5 days (see Figure 3). SN 2024uwq, like SN 2016gkg and SN 2011fu, exhibits a second maximum that is brighter than or comparable to the initial maximum, a characteristic that differentiates them from SN 1993J and SN 2013df, whose secondary peaks are significantly less luminous. Following the second maximum, SN 2024uwq demonstrates a relatively slow decline, comparable only to SN 2011fu, while most other SNe in the sample show much faster timescales of decline. The slow decline rate observed after the second maximum is consistent with radioactive heating from the decay of ^{56}Ni, which powers the later light-curve phases in all SNe IIb. For SN 2024uwq, the particularly gradual decline suggests a relatively high ^{56}Ni or enhanced trapping of gamma rays, as discussed in Section 4.3.

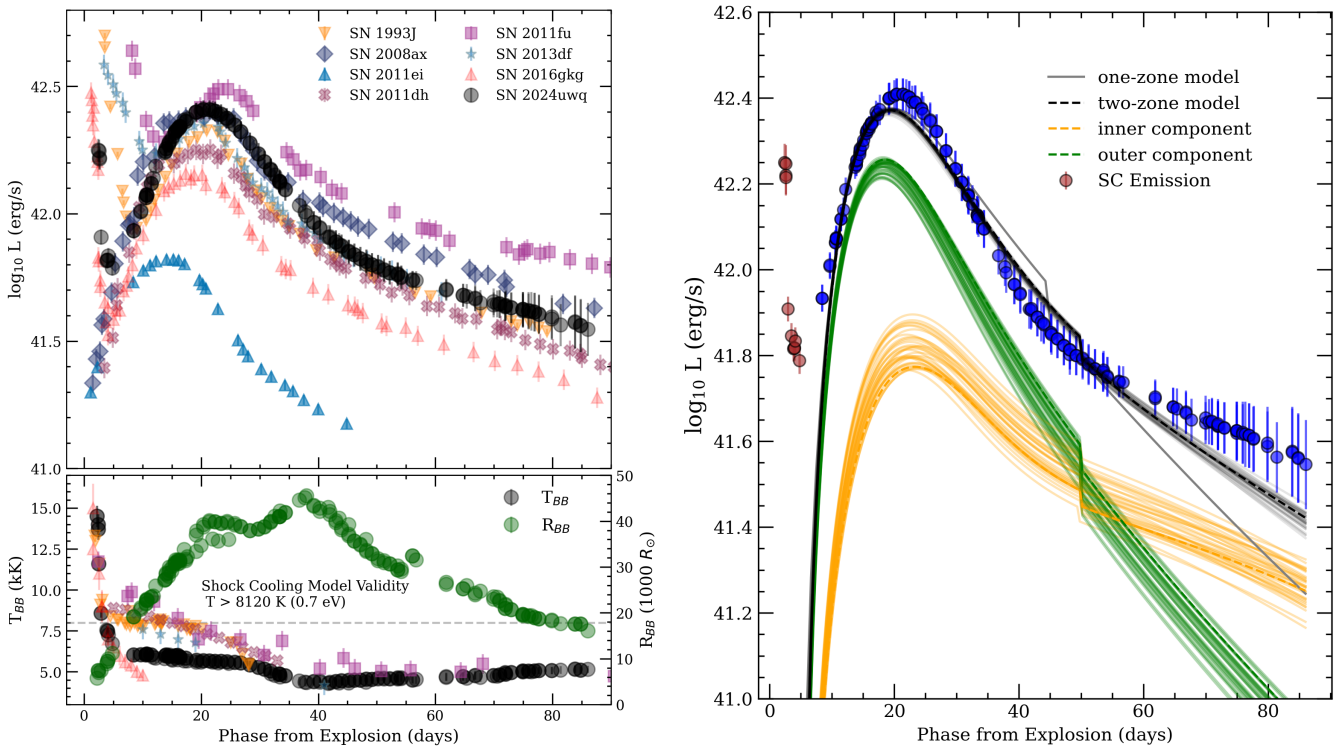

Figure 4. Left: bolometric light curve of SN 2024uwq, along with the evolution of temperature (black) and photospheric radius (green). The bolometric light curve and blackbody temperatures $T_{\rm BB}$ of SN 2024uwq are compared with those of other SNe IIb in the literature when available. In the bottom $T_{\rm BB}-R_{\rm BB}$ panel, the overplotted comparison points represent $T_{\rm BB}$ only. Shock cooling models are valid only for data where the $T_{\rm BB}$ is greater than 8120 K or 0.7 eV (see N. Sapir & E. Waxman 2017) Right: bolometric light-curve fit with a two-component Arnett model using MCMC. Black and gray lines depict two- and one-component models, respectively (150 random draws from the posterior); orange and green trace inner and outer ejecta contributions, respectively. Observational data are shown in blue with 1σ uncertainities.

4.2. Color Evolution

In Figure 3, we present the extinction-corrected color evolution of SN 2024uwq in $U-B$, $B-V$, $g-r$, and $r-i$, compared to well-studied SNe IIb. During the earliest phases (2 − 5 days), SN 2024uwq exhibits a blueward color evolution (lasts $\leqslant$ 1 day) followed by rapid reddening, particularly in $U-B$, $B-V$, and $g-r$ but less pronounced in $r-i$. This early rapid redward evolution is indicative of shock cooling. SN 2024uwq at this phase lacks the early red excess in $U-B$, as observed for SN 2008ax and SN 2011dh, which are associated with compact progenitors dominated by radioactive heating even at earlier phases (A. Pastorello et al. 2008; I. Arcavi et al. 2011). The $U-B$ colors of SN 2024uwq closely resemble those of SN 1993J, SN 2013df, and SN 2016gkg.

The $B-V$ and $g-r$ colors of SN 2024uwq initially exhibit a blueward evolution until the second maximum (20 days) before transitioning to a reddening phase. This behavior is consistent with most SNe IIb, though SN 2024uwq maintains a systematically bluer color nearly up to 50 days past explosion. The $r-i$ evolution of SN 2024uwq shows gradual reddening up to 60 days, followed by a slight blueward trend, with values higher than those of SN 1993J and SN 2011fu but comparable to SN 2016gkg and SN 2008ax (M. W. Richmond et al. 1994; A. Pastorello et al. 2008; A. Morales-Garoffolo et al. 2015; L. Tartaglia et al. 2017); see Figure 3.

4.3. Bolometric Analysis

We used photometric measurements corrected for extinction in all available passbands to construct the bolometric light curve of SN 2024uwq, employing `SuperBol`[19] (M. Nicholl 2018). Given the critical role of UV observations in constraining blackbody fits, but its sparser sampling during the rapidly evolving shock cooling and subsequent rise, we interpolated light curves using higher-order polynomials, approximately fifth to eighth order, with the specific order varying by band based on light-curve evolution. Each observed epoch was fit to a blackbody spectral energy distribution (SED) from where we directly calculate the blackbody temperatures and blackbody radii as functions of time. The bolometric luminosities were then computed from the fitted blackbody radii ($R_{\rm BB}$) and temperatures ($T_{\rm BB}$) using the Stefan−Boltzmann law. We compare the bolometric luminosities of SN 2024uwq with those of SN 1993J, SN 2008ax, SN 2011ei, SN 2011dh, SN 2011fu, SN 2013df, and SN 2016gkg, all well-studied SNe IIb with robust data sets in the literature. These events were selected for their well-sampled early multiwavelength observations and relative proximity ($\leqslant$80 Mpc), enabling reliable bolometric light curves. The bolometric light curve of SN 2024uwq, along with temperature and photospheric radius, is shown in Figure 4. We make a validity cut on the SCE time range based on the temperatures $\geqslant$8120 K (0.7 eV), as described in N. Sapir & E. Waxman (2017) and J. Morag et al. (2023; see Equation A3). The bolometric luminosity of the first observation of SN 2024uwq is measured to be $\log L$ (erg s^{-1}) = 42.250 ± 0.031. Following the initial shock cooling phase, the bolometric luminosity reaches a second maximum, measured at $\log L$ (erg s^{-1}) = 42.409 ± 0.037. The bolometric luminosity of the second

[19] https://github.com/mnicholl/superbol

maximum of SN 2024uwq is consistent with the upper range observed in SNe IIb, with SN 2011fu peaking at slightly higher luminosity in the comparison sample as seen in Figure 4 (A. Morales-Garoffolo et al. 2015). SN 1993J, SN 2008ax, and SN 2013df show slightly lower values ($\log L$ (erg s^{-1})≈ 42.37–42.38), while SN 2011ei, SN 2016gkg, and SN 2011dh are among the least luminous in the sample, with $\log L$ (erg s^{-1}) ≈ 41.8, 42.13 0.11, and 42.15 0.02, respectively (D. Milisavljevic et al. 2013; I. Arcavi et al. 2011; L. Tartaglia et al. 2017). The effective temperature of SN 2024uwq evolves from a temperature of T 15 kK during the first observation, with a fast decrease to 6 kK up to 10 days and reaching around 5.6 kK during the second light-curve maximum. The temperature evolution is similar to that of SN 2016gkg, where the initial observation yielded T 13 kK, rapidly decreasing to 7.9 kK (L. Tartaglia et al. 2017). The photospheric radius of SN 2024uwq during the initial peak is estimated to be $R_{\rm phot}$ 7000 $R_\odot$, expanding to $\geqslant 4 \times 10^4$ $R_\odot$ at approximately 40 days, after which it gradually recedes as SN 2024uwq further evolves.

4.4. ^{56}Ni Mass Estimates

We model the second peak of the bolometric light curve of SN 2024uwq using both one- and two-component variations of the analytical framework adapted from W. D. Arnett (1982) and S. Valenti et al. (2008), originally developed for SNe Ia and subsequently extended to SESNe (J. D. Lyman et al. 2016; Y. Dong et al. 2024). The one-component model assumes a single homogeneous ejecta structure, where the photospheric phase luminosity $L_{\rm bol,phot}(t)$ is powered by radioactive decay of ^{56}Ni and ^{56}Co, with gamma-ray leakage $\Gamma(z)$ integrated over time (Equation (4); S. Valenti et al. 2008). The characteristic timescale $\tau_m \propto (M_{\rm ej}^3/E_k)^{1/4}$ depends on the mass of the ejecta $M_{\rm ej}$, the kinetic energy E_k, and the constants $\kappa_{\rm opt} = 0.07$ cm^2 g^{-1}, = 13.8. The two-component model for SESNe is motivated by the inability of single-zone models to reconcile photospheric phase luminosity (dominated by outer low-density ejecta with rapid cooling) and nebular phase emission (powered by inner dense ejecta with enhanced gamma-ray trapping), as well as the need for ^{56}Ni mixing observed in SESNe. Here $L_{\rm bol,tot}(t)$ becomes the sum of contributions from both components:

$$L_{\rm bol,tot}^{\rm 2\text{-}comp}(t) = L_{\rm phot}(t) + L_{\rm neb}(t), \quad (1)$$

where $L_{\rm phot}(t)$ and $L_{\rm neb}(t)$ retain the formalism described in S. Valenti et al. (2008) and E. Chatzopoulos et al. (2012).

We constrain the time when shock cooling ends with respect to explosion epoch t_s, ejecta mass $M_{\rm ej}$, nickel mass $M_{\rm 56Ni}$, kinetic energy E_k, and inner mass fraction $f_{\rm inner}$ using Markov Chain Monte Carlo (MCMC) sampling and adopting uniform priors for the physical parameters. We fit the bolometric light curve from −10 to +15 days and >60 days after maximum, epochs that best represent photospheric and nebular phases of SN 2024uwq's evolution. We assume that the end of the shock cooling phase coincides with the onset of the radioactive-decay-powered component. The shock cooling end time, t_s, is treated as a free parameter in our MCMC modeling and is inferred from the fit to the bolometric light curve. This yields a best-fit value of $t_s = 4.94^{+0.042}_{-0.079}$ days, consistent with our assumed explosion epoch (see Figure 4). The best-fit parameters give $M_{\rm 56Ni} = 0.098^{+0.001}_{-0.001}\,M_\odot$, $M_{\rm ej} = 3.00^{+0.103}_{-0.089}\,M_\odot$, $E_{k,\rm total} = 2.75^{+0.02}_{-0.03} \times 10^{51}$ erg, and $f_{\rm inner} = 0.33$ 0.03, consistent with SESN population studies (J. D. Lyman et al. 2016; F. Taddia et al. 2018). Simplified one- and two-zone models struggle to match the observed luminosity beyond 60 days (Figure 4). While the two-zone model provides a more physically motivated framework by accounting for inner and outer ejecta components, it does not significantly outperform the one-zone model at late times. Increasing the inner ejecta density component might explain the late-time emission, and it would also broaden the primary peak, highlighting the limitations of these simplified models compared to a continuous density profile. Alternative energy sources, such as circumstellar medium interaction (e.g., R. A. Chevalier & C. Fransson 1994; T. J. Moriya et al. 2023; M. Rizzo Smith et al. 2023) or magnetar spin-down (e.g., D. Kasen & L. Bildsten 2010; S. E. Woosley 2010), have been suggested to account for the extended luminosity tail in CCSNe.

5. Spectroscopy

5.1. Optical Spectra

We show the spectral evolution of SN 2024uwq ranging from +4 to +64 days after explosion in Figure 5. The most prominent lines are identified in the figure. In the earliest spectrum, taken at +4 days, a broad P Cygni H profile is evident, along with an absorption feature of H near 4700 Å. Both the H and H absorption components exhibit flat-topped profiles, indicative of a geometrically thin, spherically expanding hydrogen shell. In this configuration, the shell emits uniformly across a range of Doppler-shifted velocities, producing a flat-topped profile owing to the equal contribution from all regions of the shell (S. E. Woosley et al. 1994; L. Dessart et al. 2013; M. González-Bañuelos et al. 2025). These early features are also seen in the spectra of SN 1993J, SN 2013df, and SN 2016gkg at similar phases (A. Morales--Garoffolo et al. 2014; L. Tartaglia et al. 2017). Additionally, the spectrum shows He I λ5876 absorption, as well as weak traces of Ca II H and K absorption at 3934 and 3968 Å. The low continuum temperature at this epoch, derived as 8500 K from a blackbody fit (see Figure 4), combined with the presence of low-ionization elements, suggests rapid cooling following shock breakout (I. Arcavi et al. 2011).

The evolution of the H and He I lines across multiple epochs is presented in Figure 6. The H line strengthens as SN 2024uwq evolves, and by +15 days a secondary component, likely He I λ6678, emerges, similar to the evolution of SN 2016gkg (L. Tartaglia et al. 2017). Strong P Cygni profiles of He I lines develop following the shock cooling phase and intensify by +23 days. The Ca II H and K P Cygni features are first discernible around +10 days, exhibiting steady growth in subsequent epochs, while the Ca II NIR triplet shows a pronounced increase in strength starting at +34 days (see Figure 5).

At epochs greater than +40 days, the H line intensity decreases by approximately a factor of two, whereas the He I lines, including 5876 Å, 6678 Å, and 7065 Å, strengthen significantly, with an enhancement factor of 2 relative to earlier spectra. The He I λλ6678 and 7065 features, absent in the early spectra, become distinctly visible at this stage, consistent with previous observations of SN 2011fu, SN 2013df, and SN 2016gkg (A. Morales-Garoffolo et al. 2015, 2014; L. Tartaglia et al. 2017).

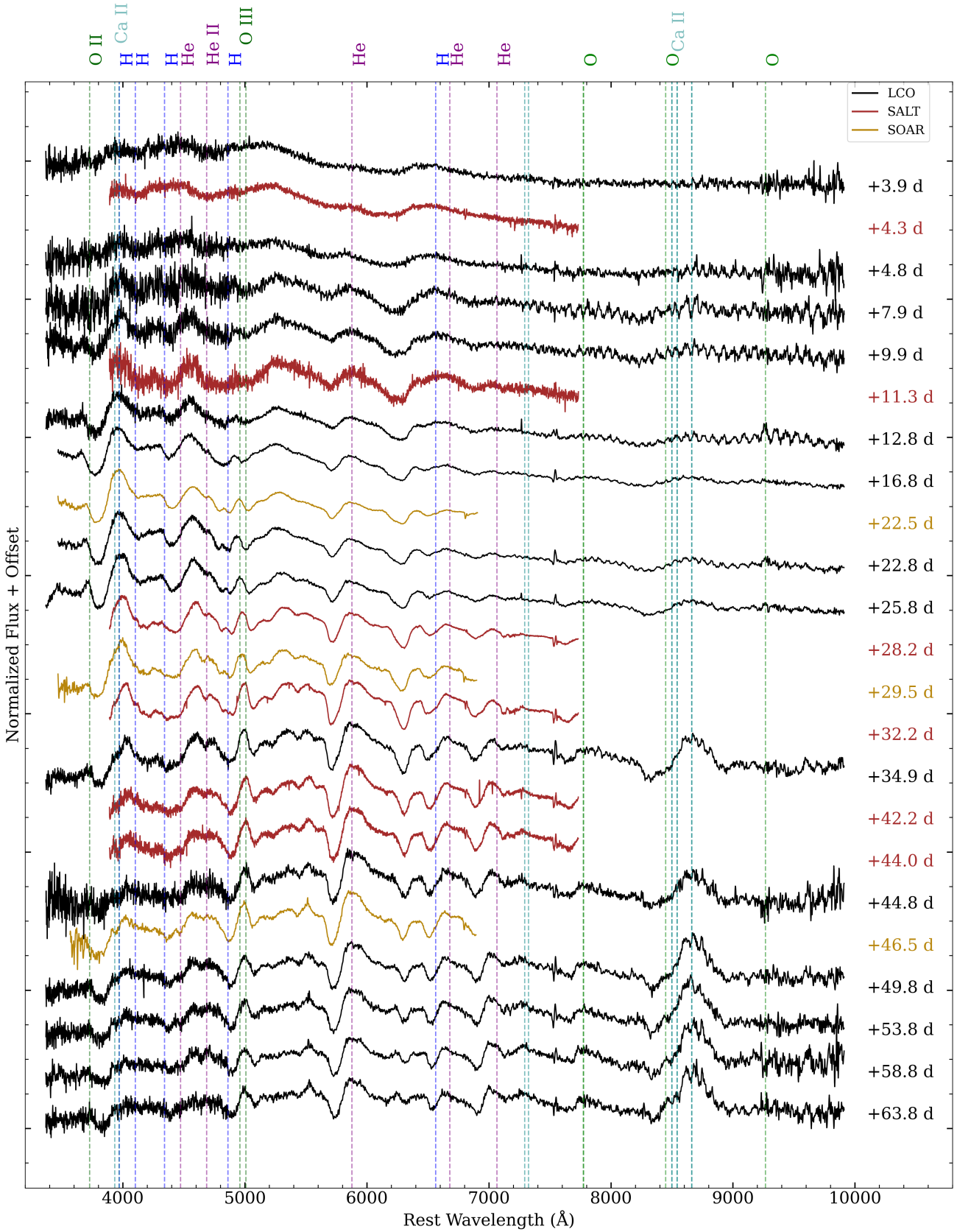

Figure 5. Optical spectra of SN 2024uwq showing temporal evolution from +4 to +64 days, with respect to our assumed explosion epoch of MJD 60558.63. The most prominent lines in the spectra are identified. Spectroscopic data used in this figure are available as data behind the figure.
(The data used to create this figure are available in the online article.)

5.2. Velocity Evolution

Figure 6 shows the evolution of the expansion velocities of H and He I for SN 2024uwq. The expansion velocities are derived from the position of the minima of the P Cygni profile of each respective line. The H velocity starts as high as 15,500 km s^{-1} at +4 days, subsequently decreasing to 10,000 km s^{-1} at +30 days. For our earliest phases, we measure the minimum of the P Cygni of the H line by fitting a Gaussian to the absorption profile, and we derive H expansion velocities, which are close to the values obtained for other SNe IIb at similar phases, including SN 2008ax, SN 2013df, SN 2011dh, and SN 2016gkg (A. Pastorello et al. 2008; A. Morales-Garoffolo et al. 2014; I. Arcavi et al. 2011). The comparison sample includes SNe IIb with well-sampled early-phase expansion velocities available in the literature, measured using similar spectroscopic techniques. For instance, SN 2016gkg H line profiles evolve in a similar range, with expansion velocities declining from 16,500 km s^{-1} at +1.70 days to 12,200 km s^{-1} at +21 days (L. Tartaglia et al. 2017). The He I λ5876 expansion velocities evolve much faster than the H . First appearing around +4 days, the expansion velocity decreases steeply from 14,000 to 7000 km s^{-1} by +15 days. With an initial rapid drop at earlier phases, the Ca II H and K expansion velocities then evolve steadily, tracking the H velocity evolution until +46 days, after which they decrease below H . For later epochs, the rate of velocity change for all three lines decreases. The H expansion velocities of SN 2024uwq are systematically higher than those of normal SNe II (e.g., 8000–12,000 km s^{-1} at comparable epochs; J. E. Andrews et al. 2024; M. Shrestha et al. 2024b), consistent with the enhanced ejecta velocities observed in SESNe.

5.3. NIR Spectroscopy

We present an NIR spectrum of SN 2024uwq at +76 days in Figure 7. The strongest feature in the spectrum is a P Cygni profile peaking around 1.0830 μm, which is due to He I. The concurrent presence of a clear P Cygni profile around 2.0581 μm confirms a significant contribution from He I, which is expected in an evolved spectrum of an SN IIb (e.g., S. Taubenberger et al. 2011; F. Bufano et al. 2014; M. Ergon et al. 2015; M. Shahbandeh et al. 2022). The He I P Cygni profile at 1.0830 μm is potentially contaminated by Paγ (1.094 μm), while the Pa (1.282 μm) absorption is not evident. SN 2024uwq exhibits absorption features at 0.9264 and 1.129 μm, consistent with O I lines commonly seen in SESNe (M. Shahbandeh et al. 2022). Several C I lines are also identified in the NIR spectra of SN 2024uwq. While weaker C I features at 0.9093 and 0.9406 μm may be blended with the nearby O I0.9264 μm line, the prominent C I1.0693 μm feature is detected and likely contributes significantly to the broad P Cygni, along with He I1.0830 μm. Most evolved NIR spectra of SESNe show an emission-like Mg I feature around 1.5 μm (with contributions from Mg I 1.4878 μm and Mg I 1.5033 μm; M. Shahbandeh et al. 2022). This feature is observed in SN 2024uwq. The emission band at 1.19 μm can likely be attributed to Si I 1.198 and 1.203 μm blended with Mg I 1.183 μm as observed for SN IIb SN 2011hs (F. Bufano et al. 2014). Similarities with

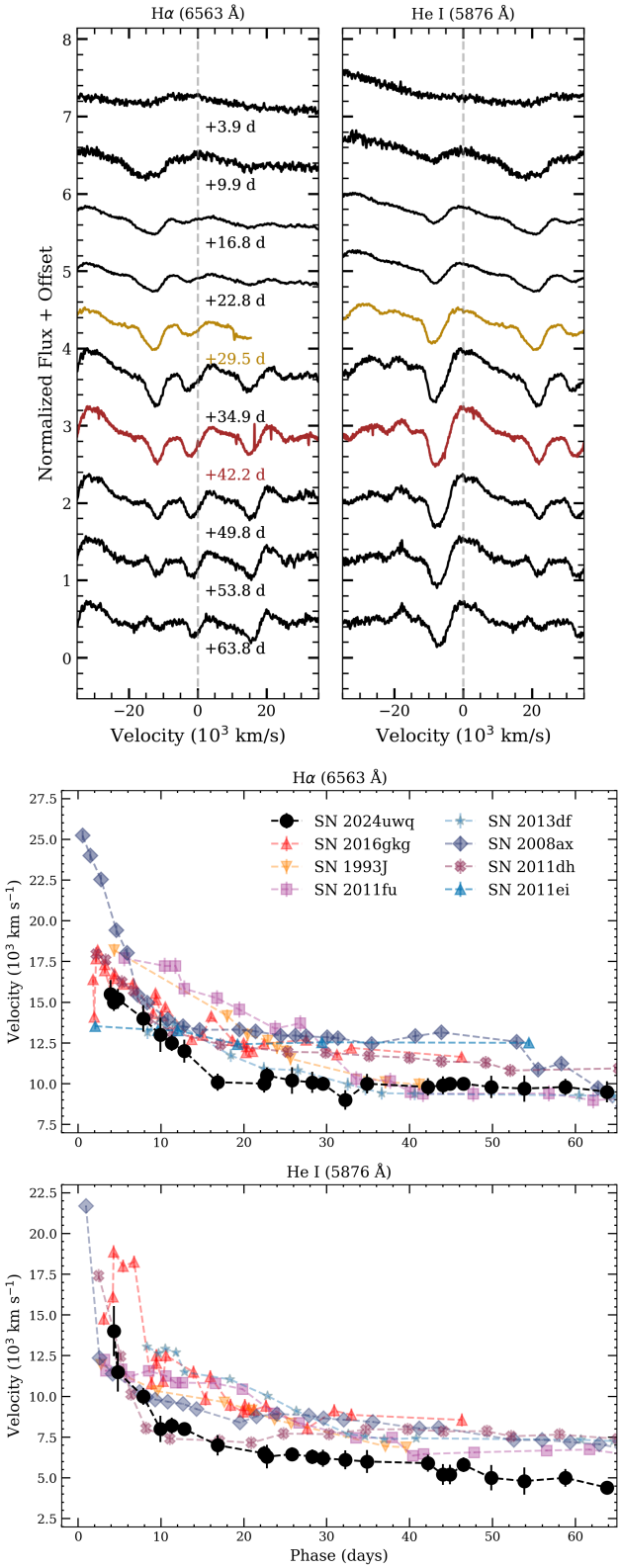

Figure 6. Top: multiepoch spectral evolution of H (λ6563) and He I (λ5876), observed between +4 and +64 days. The H emission-line profile evolution is strongly affected by He I λ6678 line emergence. Bottom: velocity evolution of SN 2024uwq derived from P Cygni minima of H and He I, shown relative to explosion epoch and in comparison to other SNe IIb.

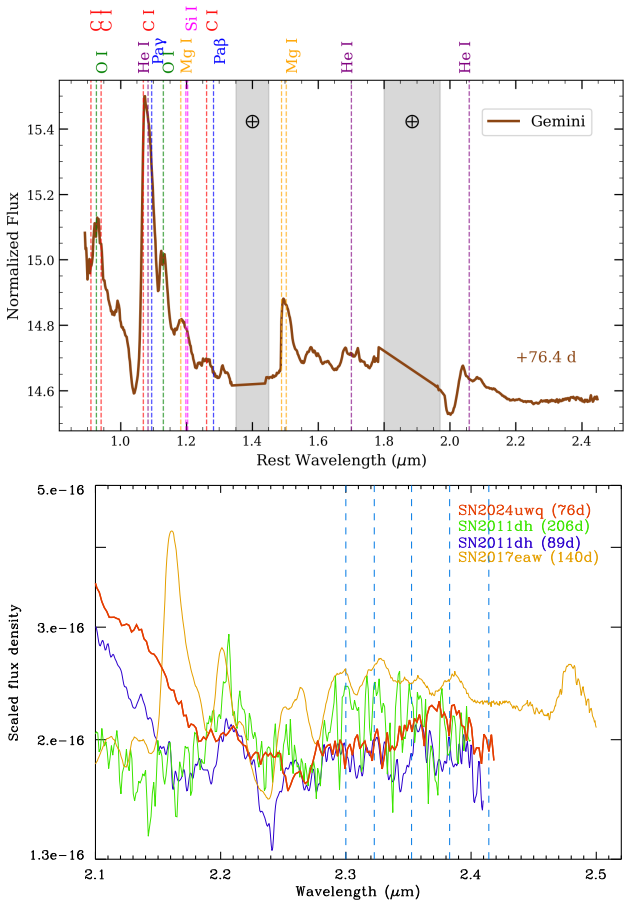

Figure 7. Top: NIR spectra of SN 2024uwq at +76 days obtained using Gemini F-2. The gray bands mark the regions with high telluric absorptions and emissions. Bottom: The CO first-overtone feature of SN 2024uwq (in red) shows strong resemblance to those observed in the SN IIb SN 2011dh and is also compared with those of the SN IIP SN 2017eaw. The vertical dashed lines mark the band heads of $\Delta v = 2$ transitions.

(The data used to create this figure are available in the online article.)

other SNe IIb at NIR wavelengths further confirms the classification of SN 2024uwq.

Figure 7 shows that the first-overtone CO (2.25–2.45 μm) is likely detected in the NIR spectra of SN 2024uwq. The presence of the first-overtone CO feature indicates the formation of CO molecules as the ejecta cool, a process that can subsequently lead to dust formation. The CO feature in SN 2024uwq bears some resemblance to that observed in the SN IIb SN 2011dh (M. Ergon et al. 2015). In SN 2011dh, the CO emission observed at 206 days post-explosion was inferred to have a temperature of approximately 2300 K and an expansion velocity of 1500 km s^{-1} (M. Ergon et al. 2015). Compared to the SN IIP SN 2017eaw, the CO band heads in SN 2024uwq appear less distinct.

5.4. Comparison to Other SNe IIb

We compare the optical spectra of SN 2024uwq at +4, +20, and +46 days with those of SN 1993J, SN 2008ax, SN 2011fu, SN 2011ei, SN 2011dh, SN 2013df, and SN 2016gkg at similar phases in Figure 8. These comparison SNe were selected based

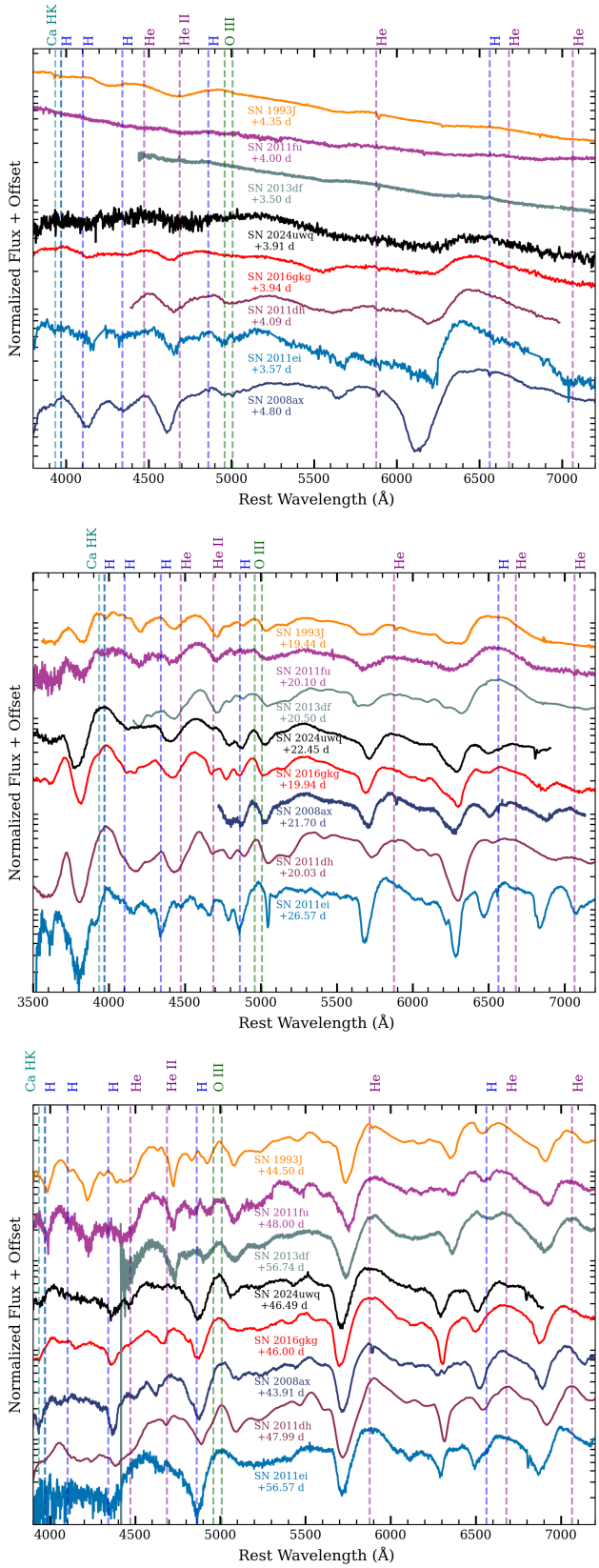

Figure 8. Comparison of the optical spectra of SN 2024uwq at +4 days (top), +20 days (middle), and +46 days (bottom) with other SNe IIb. The spectra have been redshift corrected and shifted vertically for clarity.

on the availability of well-sampled optical spectra at comparable epochs. The sample spans a range of SN IIb progenitor properties, enabling a contextual analysis of SN 2024uwq's spectral evolution within the broader diversity of the class. All data for the SN IIb comparison plot were downloaded from WISeRep (O. Yaron & A. Gal-Yam 2012). The early-phase spectra of SNe IIb, shown in the top panel, exhibit significant diversity. SN 1993J, SN 2011fu, and SN 2013df display a blue, almost featureless continuum with shallow hydrogen and helium lines (T. Matheson et al. 2000; A. Morales-Garoffolo et al. 2015, 2014). In early-time spectra, the continuum is primarily shaped by shock-heated material cooling and radiating as a blackbody. In progenitors with extended envelopes, this shock cooling phase lasts longer, producing a hot, blue continuum that can dilute or obscure line features. In contrast, SN 2008ax, SN 2011ei, and SN 2011dh are redder, characterized by stronger "saw-toothed" H spectral features. This profile, with a steep blue edge and extended red wing, reflects high-velocity hydrogen in the outer ejecta and becomes prominent once the shock-heated continuum fades. A smaller progenitor radius leads to a shorter shock cooling phase, allowing strong H absorption to dominate the early spectrum. The presence of a strong, structured H profile at early times is therefore consistent with a progenitor that is compact/significantly lacks an extended hydrogen envelope (A. Pastorello et al. 2008; I. Arcavi et al. 2011; D. Milisavljevic et al. 2013). SN 2024uwq evolves relatively similarly to SN 2016gkg, showing a blue continuum and stronger Balmer features in its earliest spectra compared to SN 1993J, SN 2011fu, and SN 2013df (L. Tartaglia et al. 2017).

At +20 days, all spectra exhibit more prominent He I λ5876 and Balmer features, as shown in the middle panel. This phase is close to the secondary peak for SN 2024uwq, after the initial decline in the light curve due to shock cooling. SN 2024uwq and SN 2016gkg display stronger He I features compared to other SNe, except for SN 2011ei and SN 2008ax, which show the strongest He I P Cygni profiles within just weeks of explosion (R. Chornock et al. 2011; D. Milisavljevic et al. 2013; L. Tartaglia et al. 2017). The line profiles of SN 2011fu evolve coherently, resembling those observed in SN 1993J and SN 2013df at this phase. The H line profile in SN 2024uwq and SN 2016gkg at this phase starts to develop two components, contrasting with the single-component profiles observed in SN 1993J, SN 2011fu, and SN 2013df, possibly due to the development of the strong nearby He I λ6678. At this phase, blueshifted H absorption is strongest in SN 2011dh, but the secondary absorption component is less pronounced compared to SN 2008ax, SN 2016gkg, and SN 2024uwq. Strong Ca II H and K features develop for SN 2024uwq, SN 2016gkg, and SN 1993J; however, the absorptions in SN 2011ei and SN 2011dh remain the strongest among the sample (R. Barbon et al. 1995; D. Milisavljevic et al. 2013; M. Ergon et al. 2014; I. Shivvers et al. 2019).

The bottom panel shows the spectra of all SNe at around +46 days, at which point they start to become redder. He I is the dominant line profile in the spectra, with weakening strengths of H . SN 2008ax shows a weak or no blueshifted H component at this phase. SN 2011fu shows the least strength in He I and H as compared to the other SNe in the sample. The O [III] $\lambda\lambda$4959, 5007 lines in all SNe strengthen compared to +20 days. SN 2016gkg shows broader He I profiles as compared to SN 2024uwq, indicating higher expansion velocities. All SNe also show He I $\lambda\lambda$6678 and 7065 in their optical spectra at this phase (T. Matheson et al. 2000; M. Modjaz et al. 2014; I. Shivvers et al. 2019). Overall, SN 2024uwq's spectral evolution closely resembles that of SN 2016gkg and SN 2013df, both of which exhibit early shock cooling signatures, in contrast to SNe 2008ax, SN 2011ei, and SN 2011dh, which lack this early light-curve feature.

6. Shock Cooling Emission Modeling

Several models have been developed over a decade to analytically describe the early SCE in CCSNe, encompassing both the "planar" and "spherical" phases of the cooling. The planar phase, where the emitting shell is significantly thinner than the stellar radius, has been modeled through exact and approximate analytic solutions (N. Sapir et al. 2011; B. Katz et al. 2012; N. Sapir et al. 2013). As the emission progresses into the spherical phase, characterized by shell expansion to radii much larger than the star, solutions have been provided by E. Nakar & R. Sari (2010), I. Rabinak & E. Waxman (2011), E. Nakar & A. L. Piro (2014), A. L. Piro (2015), N. Sapir & E. Waxman (2017), T. Shussman et al. (2016), and A. L. Piro et al. (2021).

Most spherical phase models rely on polytropic envelope structures, with A. L. Piro et al. (2021, hereafter P21) introducing a broken power-law representation of the density profile, applicable to shock breakout conditions. Interestingly, N. Sapir & E. Waxman (2017, hereafter SW17) demonstrated that SCE is relatively insensitive to the polytropic index and exhibits only a weak dependence on the progenitor density structure. Opacity effects, particularly those from bound–free and bound–bound transitions, play a key role in shaping the emitted radiation. While I. Rabinak & E. Waxman (2011) and N. Sapir & E. Waxman (2017) incorporated detailed contributions of opacity in their analysis, E. Nakar & R. Sari (2010) and T. Shussman et al. (2016) used simplified treatments of bound–free opacity in hydrogen. The spherical phase models generally describe emission arising from the outermost layers of the envelope, with N. Sapir & E. Waxman (2017) extending these descriptions to later times by incorporating numerical simulations that account for radiation from deeper layers with complex density profiles. The transition from the planar to the spherical phase has also been explored. T. Shussman et al. (2016) developed an interpolation model for this transition and showed how they can be calibrated against numerical results.

Recent refinements to shock cooling models by J. Morag et al. (2023, hereafter MSW23) use similar interpolation methods while calibrating against hydrodynamic simulations covering a broad range of progenitor properties. MSW23 combines solutions from N. Sapir et al. (2011) and B. Katz et al. (2012) for the planar phase with those of I. Rabinak & E. Waxman (2011) and SW17 for the spherical phase. This model is then calibrated against numerical hydrodynamic simulations spanning explosion energies of 10^{50}–10^{52} erg and progenitor properties such as masses of 2–40 $M_{\odot}$, radii of 3×10^{12} cm to 10^{14} cm, core-to-envelope mass ratios of $10^{-0.1}$ to $10^{0.1}$, and metallicities of 0.1–1 $Z_{\odot}$. These simulations assume local thermodynamic equilibrium and diffusion-based radiation transport with a constant electron scattering opacity ($0.34\,\mathrm{cm^2\,g^{-1}}$) , which provides accurate results for highly ionized plasma ($T \geqslant 0.7$ eV), as demonstrated by SW17. The methods described in MSW23 account for line-blanketing effects and have been applied to modeling early CCSN light curves (G. Hosseinzadeh et al. 2023; I. Irani et al. 2024;

Table 2
Summary of Parameter Priors and Best-fit Values for the Four Models

Parameter	Prior[a]			Best-fit Values[b]				Units
	Shape	Min/μ	Max/σ	SW17 ($n = 1.5$)	SW17 ($n = 3$)	P21	MSW23	
Progenitor radius (R)	Uniform	0	100	$35.71^{+7.14}_{-5.71}$	$50.0^{+14.28}_{-8.57}$	14.61 0.36	57.14 7.20	$R_\odot$
Envelope mass (M_e)	Uniform	0	10	$0.7^{+0.2}_{-0.3}$	$0.8^{+0.1}_{-0.2}$	$1.35^{+1.97}_{-0.87}$	$0.7^{+0.2}_{-0.3}$	$M_\odot$
Shock velocity (v_s)	Uniform	0	10	$0.60^{+0.3}_{-0.2}$	$0.67^{+0.3}_{-0.2}$	$2.02^{+0.32}_{-0.24}$	$0.51^{+0.4}_{-0.02}$	10^4 km s^{-1}
Explosion Time (t_0)	Uniform	60558.0	60560.5	$60558.90^{+0.07}_{-0.18}$	$60558.80^{+0.1}_{-0.3}$	60560.10 0.01	$60559.30^{+0.1}_{-0.2}$	MJD
Ejecta mass × factor[c] ($f_\rho M$)	Uniform	3	100	50^{+30}_{-40}	60 30	⋯	60 30	$M_\odot$
Intrinsic scatter (σ)[d]	Half-Gaussian	0	100	$6.8^{+0.9}_{-0.8}$	$7.8^{+1.2}_{-0.9}$	⋯	$3.4^{+0.5}_{-0.4}$	⋯

Notes.
[a] Prior column lists the minimum and maximum for a uniform distribution, and the mean and standard deviation for a Gaussian distribution.
[b] Best-fit values represent the 16th, 50th, and 84th percentiles of the posterior distribution. SW17, P21, and MSW23 are shock cooling models detailed in N. Sapir & E. Waxman (2017), A. L. Piro et al. (2021), and J. Morag et al. (2023), respectively.
[c] The ejecta mass does not have a strong effect on the early shock cooling part of the light curve. Therefore, this parameter is essentially unconstrained.
[d] The P21 model was fit using the `shock cooling-curve` package (P. Venkatraman & W. Jacobson-Galán 2024), while the SW17 and MSW23 models were employed via the Light Curve Fitting package (G. Hosseinzadeh et al. 2024).

N. Meza-Retamal et al. 2024; M. Shrestha et al. 2024b). It is to be noted that these models are subject to systematic uncertainties arising from assumptions such as constant opacity, simplified density structures, and the omission of time-dependent ionization.

We analyze the early multiwavelength data set of SN 2024uwq, displaying SCE by fitting it to the models described in SW17, P21, and MSW23. The `shock cooling-curve` package (P. Venkatraman & W. Jacobson-Galán 2024) is employed to fit the P21 model, while the SW17 and MSW23 models are fit to the early light curve using an MCMC routine implemented in the Light Curve Fitting package (G. Hosseinzadeh et al. 2024). For the SW17 model, we consider two polytropic indices ($n = 3/2$ and $n = 3$), corresponding to convective and radiative envelopes, respectively. The MCMC routine is utilized to fit the following parameters across all four models: progenitor radius (R), shock velocity scale (v_s), and envelope mass ($M_{\rm env}$). For the model fits implemented using Light Curve Fitting, we additionally incorporate an intrinsic scatter term (σ) to account for scatter around the model and the potential underestimation of photometric uncertainties. The observed error bars are scaled by a factor of $\sqrt{1+\sigma^2}$. An additional parameter, the product of the total ejecta mass and a constant of order unity (f_ρ, hereafter referred to as "scaled ejecta mass" $f_\rho M$), is included; however, the ejecta mass and density profile exhibit minimal influence on the light curve, rendering this parameter effectively unconstrained.

To ensure the validity of the data in accordance with the models, we select observations taken within the first 3.5 days after the explosion, where the effective temperature ($T_{\rm eff}$) is more than 0.7 eV, since this regime is well described by the SCE models under consideration. We performed MCMC sampling using 100 walkers initialized across the parameter space. The chains were run for 5000 steps to ensure convergence, which was assessed through visual inspection of the chain histories and by ensuring that the autocorrelation time indicated sufficient mixing of the chains. An additional 1000 steps were performed to sample the posterior distribution thoroughly. The adopted priors and derived best-fit parameter values are summarized in Table 2, and the resulting best-fit model is presented in Figure 9. We analyze these results and discuss their implications for progenitor scenarios in the next section.

7. Results and Discussion

All shock cooling models applied in this work reproduce the early observations of SN 2024uwq reasonably well, with a few notable distinctions. As seen in Figure 9, each model predicts an early UV/optical peak followed by a decline, which is steeper in the UV bands (e.g., *W2*, *M2*, *W1*, *U*) compared to the subtler decline in optical passbands (*B*, *g*, *V*, *r*, *o*, *i*). The models diverge in their ability to match the earliest UV detections and the inferred explosion epochs. The P21 model yields an explosion epoch closest to the first ATLAS *o*-band detection, whereas the SW17 ($n = 1.5$ [convective] and $n = 3$ [radiative]) and MSW23 models predict earlier onset of shock cooling signatures compared to the ATLAS *o*-band detection. The MSW23 model provides the most consistent fit to the earliest ATLAS *o*-band detections in comparison with the other models. Both the SW17 models overpredict fluxes in the earliest Swift UV bands, whereas the P21 model underestimates UV fluxes at $t > 1.5$ days. The MSW23 model fits the UV light-curve morphology with the least intrinsic scatter, in comparison to SW17 models. The steep density gradients as assumed in P21 favor compact progenitors (with R 14.6 $R_\odot$), while models with gradual density profiles (MSW23) align with more extended progenitors (up to R 57 $R_\odot$). The tighter constraints in P21 arise from nonexclusion of the intrinsic scatter parameter that reflects the systematic uncertainties from unmodeled envelope inhomogeneities or density gradients, whereas the other models adopt broader priors for σ, reflecting more conservative error estimates. All of the models consistently fit the optical data well, underscoring the importance of early UV observations in disentangling the progenitor structures by breaking any known degeneracies.

The inferred progenitor properties are inconsistent with those of classical RSGs, which typically have radii $R \gtrsim 100\,R_\odot$ (e.g., G. Hosseinzadeh et al. 2023; J. E. Andrews et al. 2024; N. Meza-Retamal et al. 2024; M. Shrestha et al. 2024a). The envelope mass for SN 2024uwq (M_e 0.7–1.4 $M_\odot$) is larger than that for SN 1993J, M_e 0.4 $M_\odot$ (S. E. Woosley et al. 1994), which explains the persistence of weak H lines at >50 days. This estimate is, however, smaller than the hydrogen-rich envelopes of typical SNe IIP ($M_e \gtrsim 4$–$10\,M_\odot$; A. Jerkstrand

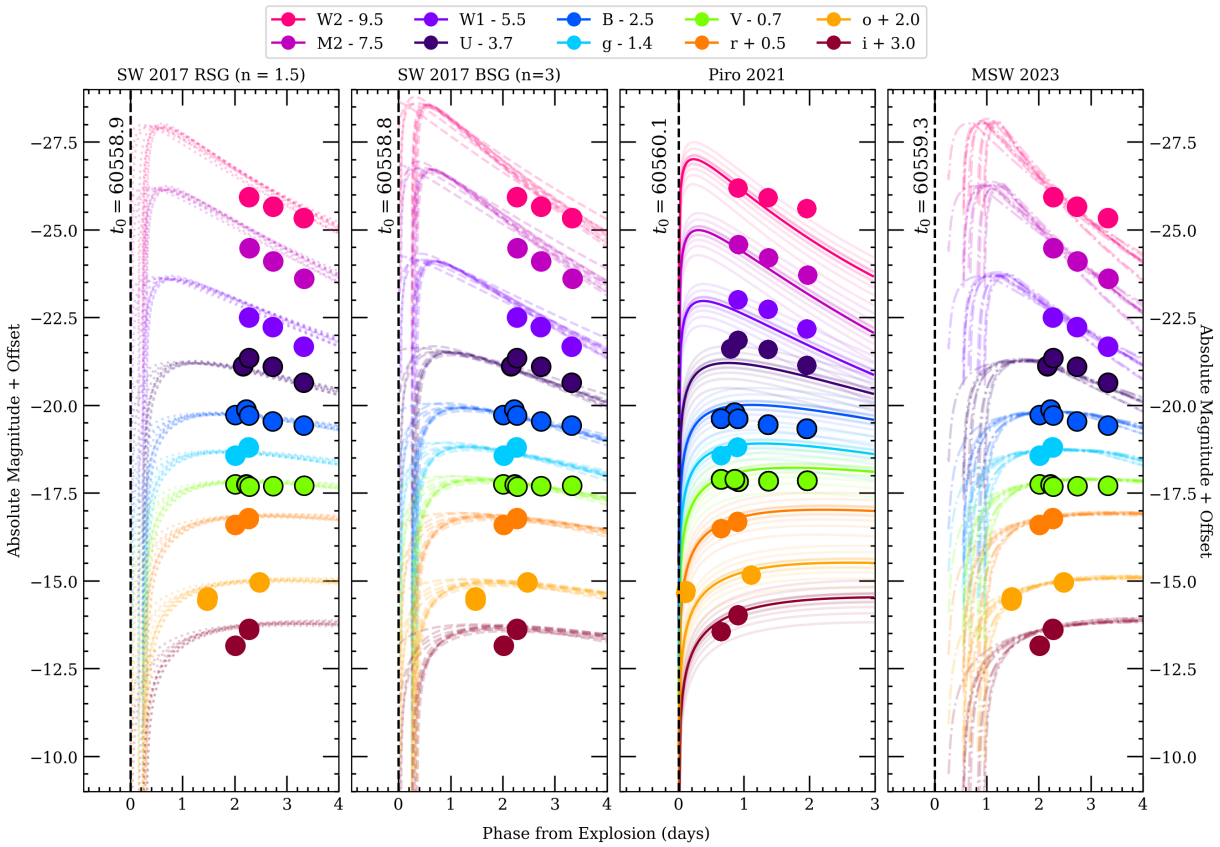

Figure 9. Early-time light curve of SN 2024uwq with shock cooling model fits. Each panel represents the individual shock cooling model. The family of model light curves in each panel represents 50 models randomly sampled from the derived posterior probability distribution in individual bands. The best-fit values and prior distributions of the physical parameters for each model considered in this work are listed in Table 2.

et al. 2012; L. Dessart et al. 2013; T. Sukhbold et al. 2018). This intermediate value suggests a progenitor that retained a modest hydrogen envelope prior to explosion, likely stripped via binary interactions. The results from the best-fit models therefore constrain SN 2024uwq's progenitor to likely be a stripped blue supergiant (BSG)/YSG with a radius $R = 14.6$–$57.1\,R_{\odot}$ and a hydrogen envelope mass $M_e = 0.7$–$1.35\,M_{\odot}$.

Unlike some well-studied SNe IIb (e.g., SN 1993J, G. Aldering et al. 1994; SN 2008ax, R. M. Crockett et al. 2008; SN 2011dh, J. R. Maund et al. 2011; SN 2013df, S. D. Van Dyk et al. 2014; SN 2016gkg, C. D. Kilpatrick et al. 2022; SN 2024abfo, A. Reguitti et al. 2025), there is no pre-explosion imaging of the SN 2024uwq progenitor to directly constrain its pre-SN luminosity or radius. Nonetheless, the inferred properties align with the observed continuum of SN IIb progenitors, ranging from ultrastripped systems like SN 2011ei ($M_e < 0.1\,M_{\odot}$; D. Milisavljevic et al. 2013) to the moderately stripped SN 1993J ($M_e < 0.4\,M_{\odot}$; S. E. Woosley et al. 1994), to minimally stripped cases like SN 2017jgh ($M_e < 1\,M_{\odot}$; P. Armstrong et al. 2021). Standard stellar evolution models that invoke binaries predict extended RSGs for stars with $\geqslant 1\,M_{\odot}$ hydrogen at collapse, as compared to the compact BSG/YSG inferred for SN 2024uwq from analytical model fits (S.-C. Yoon et al. 2017). This makes SN 2024uwq an intriguing case, potentially indicating a continuous evolutionary spectrum between canonical SNe II and SESNe. This continuum is theorized to reflect the efficiency of mass transfer in binary systems, where initial orbital parameters (i.e., mass ratios or orbital periods) or less efficient stripping could result in the larger envelope mass observed here (J. S. W. Claeys et al. 2011; N. Smith et al. 2011; N. Sravan et al. 2020).

Shock velocity estimates from model fits support a YSG/BSG progenitor scenario. The high velocity obtained from the P21 model ($v_s = 2.02^{+0.32}_{-0.24} \times 10^4$ km s^{-1}) is consistent with early-time H expansion velocities ($v_{\rm H}$ 15,500 km s^{-1}) and aligns with expectations for more compact progenitors than RSGs, where the shock propagates through a dense, steeply stratified envelope. RSGs, in contrast, exhibit slower shock velocities ($v_s \lesssim 10^4$ km s^{-1}) owing to their extended, low-density envelopes (J. E. Andrews et al. 2024; M. Shrestha et al. 2024a). The lower velocities ($\lesssim 0.7 \times 10^4$ km s^{-1}) predicted by other shock cooling models are more consistent with later-phase He I measurements ($v_{\rm He\,I}$ 7000 km s^{-1}), which trace deeper, slower-moving ejecta. Moreover, the SW17 and MSW23 models yield v_s values that align with theoretical expectations ($v_s \approx 0.5\,v_{\rm exp}$; C. D. Matzner & C. F. McKee 1999), where $v_{\rm exp}$ represents the velocity of the outermost ejecta layers.

The two-zone Arnett model described in Section 4.3 yields an ejecta mass of $M_{\rm ej}$ $3.0\,M_{\odot}$, and when combined with a typical neutron star remnant ($1.4\,M_{\odot}$), the pre-SN mass is $4.4\,M_{\odot}$. Stellar evolution models indicate that single stars with initial (zero-age main-sequence (ZAMS)) masses of 12–20 $M_{\odot}$ develop helium cores of 4–6 $M_{\odot}$ by core collapse (S. J. Smartt 2015). This range overlaps with the inferred $M_{\rm pre-SN}$, but the retained hydrogen envelope mass ($M_{\rm env}$ 0.7–1.35 $M_{\odot}$) presents a challenge for single-star models. Radiation-driven winds in stars $<20\,M_{\odot}$ are inefficient, stripping $<0.1\,M_{\odot}$ of hydrogen (J. S. Vink et al. 2011),

which is insufficient to account for the inferred envelope mass in SN 2024uwq. At solar or subsolar metallicities, even enhanced single-star mass loss due to rotation (e.g., pulsational instabilities or eruptions) could only strip $\lesssim 0.3\,M_{\odot}$ (S.-C. Yoon et al. 2017). Given the considerations for single-star progenitors, these models require fine-tuned initial masses, metallicities, and rotations, making this scenario less probable.

Binary-driven mass loss could more naturally explain the intermediate envelope mass. Case B/C mass transfer in binaries can strip hydrogen envelopes efficiently to $M_{\rm env}$ 0.1–1.5 $M_{\odot}$ (S.-C. Yoon et al. 2017), matching with SN 2024uwq's properties. The derived $M_{\rm pre-SN} \approx 4.4\,M_{\odot}$ aligns with stripped helium cores of $M_{\rm ZAMS}$ 12–15 $M_{\odot}$ stars that were the product of binary interaction (E. Laplace et al. 2021; D. Vartanyan et al. 2021). While direct evidence for a binary companion is absent in the existing data, the intermediate $M_{\rm env}$ inferred from the shock cooling models favors binary stripping over single-star winds. Wolf–Rayet progenitors, which lose nearly their entire hydrogen envelopes ($M_{\rm env} < 0.1\,M_{\odot}$) via strong winds, are unlikely, as these systems typically produce more massive helium cores ($M_{\rm He} > 6\,M_{\odot}$) and higher explosion energies (T. Sukhbold et al. 2016), inconsistent with the inferred $M_{\rm ej}$ and shock velocities for SN 2024uwq.

We place SN 2024uwq in context with other SNe IIb in the R–$M_{\rm env}$ phase space shown in Figure 10. For SN 2024uwq, we display the best-fit progenitor radius and envelope mass obtained from all four shock cooling models explored in this work, with each marker's fill style indicating the respective model. For SNe shown in bold, both progenitor radius and envelope mass are obtained exclusively from published shock cooling analyses, allowing for a self-consistent comparison with SN 2024uwq. The remaining SNe utilize values determined through alternative approaches, such as pre-explosion imaging, late-time radio observations, or hydrodynamical modeling. R. A. Chevalier & A. M. Soderberg (2010) proposed that SNe IIb may be divided into two subgroups: extended-envelope IIb (eIIb; e.g., SN 1993J, with $M_{\rm env} > 0.1\,M_{\odot}$, $R_{\rm env}$ 10^{13} cm) and compact-envelope IIb (cIIb; e.g., SN 2008ax, with $M_{\rm env} < 0.1\,M_{\odot}$, $R_{\rm env}$ 10^{11} cm). These subtypes may represent a continuum modulated by the amount of residual hydrogen, with cIIb events potentially bridging to SNe Ib. SN 2024uwq, with intermediate progenitor properties ($M_{\rm env}$ 0.7–1.35 $M_{\odot}$, $R_{\rm env}$ 14.6–57.1 $R_{\odot}$), occupies a transitional region in this space, possibly resulting from moderate stripping in a binary system. This continuum, spanning objects like SN 2008ax (cIIb) and SN 2017jgh (eIIb), underscores varying degrees of envelope stripping, likely modulated by binary interaction efficiency.

We note that in Figure 10 there appears to be a tendency for progenitors with relatively large radii to have lower envelope masses, and vice versa. This interesting anticorrelation is seen across SNe with properties derived from a variety of methods, indicating that this observed trend is model/method independent. Seen as roughly perpendicular to the conventional stripping sequence often invoked to connect SN II and SN IIb progenitors to SN Ib/c progenitors, this could suggest that factors in addition to simple envelope removal, such as the residual hydrogen fraction, envelope mixing, binary interaction history, envelope inflation in low-mass hydrogen layers, and/or pre-SN structural changes, could play a significant role in setting the final progenitor radius and envelope structure in SNe IIb (J. S. W. Claeys et al. 2011; S.-C. Yoon et al. 2017; N. Sravan et al. 2020).

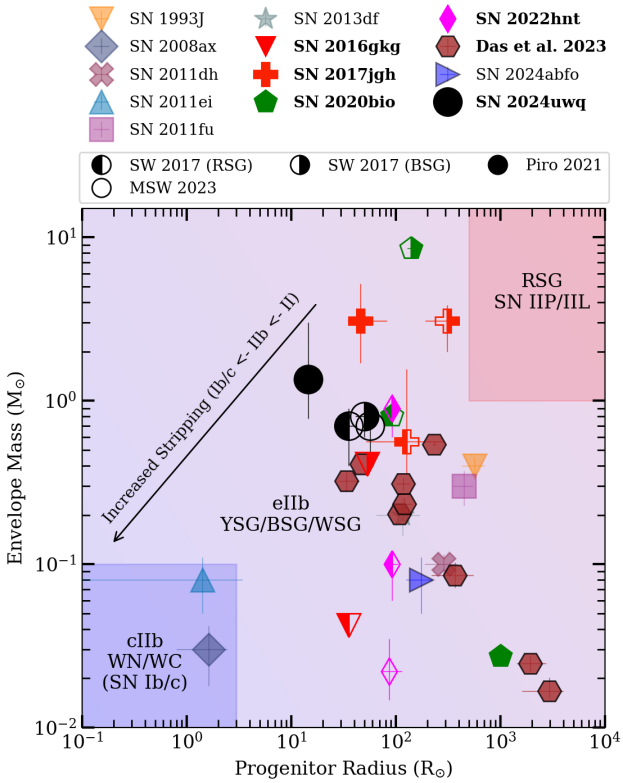

Figure 10. Progenitor radius vs. envelope mass for SNe IIb, including SN 2024uwq. All best-fit values of all four models are shown, with each filling style of the marker indicating the respective model. For the SNe highlighted in bold, where the comparison values are from shock cooling modeling, we plot the available respective model values in the literature. Published values for other SNe in this figure are obtained from S. E. Woosley et al. (1994; SN 1993J), A. Pastorello et al. (2008) and R. A. Chevalier & A. M. Soderberg (2010; SN 2008ax), M. C. Bersten et al. (2012; SN 2011dh), D. Milisavljevic et al. (2013; SN 2011ei), A. Morales-Garoffolo et al. (2015; SN 2011fu), A. Morales-Garoffolo et al. (2014; SN 2013df), I. Arcavi et al. (2017; SN 2016gkb), P. Armstrong et al. (2021; SN 2017jgh), C. Pellegrino et al. (2023; SN 2020bio), J. R. Farah et al. (2025; SN 2022hnt), and A. Reguitti et al. (2025) and K. K. Das et al. (2023; SN 2024abfo).

Detailed hydrodynamical modeling of both single stars with mass loss and interacting binary systems, combined with comprehensive observational studies, is essential to advance our understanding of the complex evolutionary pathways of massive stars and their role in shaping the diversity of SNe IIb (J. A. Goldberg et al. 2022; G. Long et al. 2022; A. Haynie & A. L. Piro 2023). Our analysis underscores the critical role of early-time UV observations in resolving the shock cooling phase of SNe. As shown in Figure 11, the inclusion of UV data significantly improves constraints on the blackbody temperature evolution, particularly at early phases when the SED peaks in the UV. Without UV coverage, temperature fits rely solely on the optical slope, resulting in larger uncertainties and potential biases.

7.1. Future Surveys and SN IIb Rates

Future time-domain surveys, including ULTRASAT, UVEX, and the Vera Rubin Observatory's LSST, will revolutionize our understanding of SESN progenitors and massive-star evolution (Ž. Ivezić et al. 2019; S. R. Kulkarni et al. 2021; Y. Shvartzvald et al. 2024). Figure 12 shows the simulated near-UV (NUV) light curves for SN 2024uwq by convolving its observed SED at each epoch with the ULTRASAT

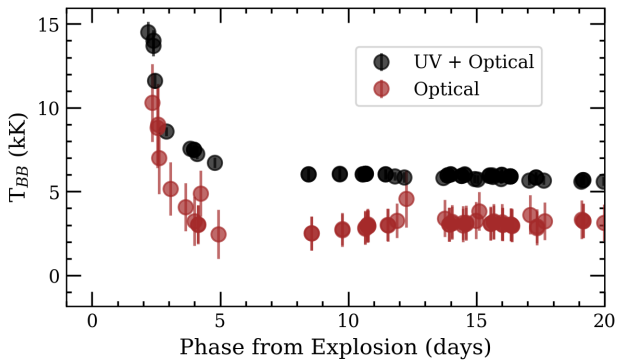

Figure 11. Evolution of the blackbody temperature ($T_{\rm BB}$) as a function of phase from explosion for UV + optical and optical-only observations. The inclusion of UV data provides better constraints on the SED peak, resulting in more accurate temperature estimates and reduced uncertainties, particularly at early times.

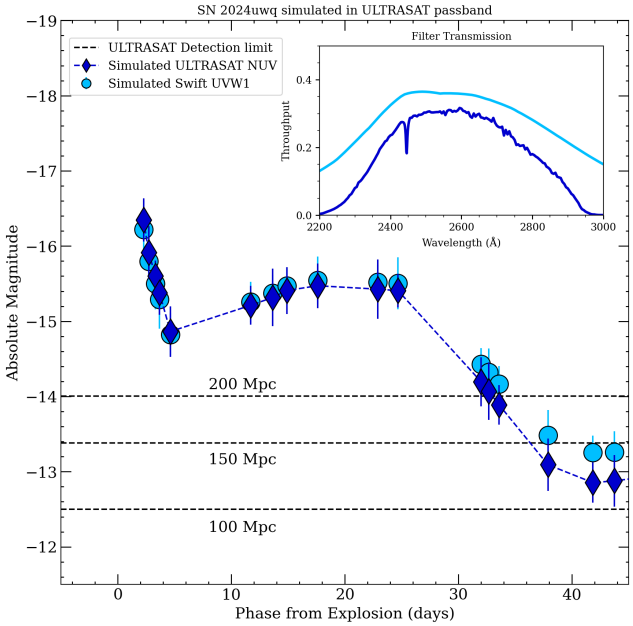

Figure 12. Simulated ULTRASAT NUV and Swift UVW1 light curves, demonstrating ULTRASAT's detectability of complete SCE phases out to 200 Mpc. Photometry was simulated using the SED of SN 2024uwq at each epoch convolved with the respective filter throughput. The error bars represent the photometric uncertainties.

and Swift UVW1 filter throughputs, demonstrating its ability to capture the complete SCE phase out to 200 Mpc. ULTRASAT's wide-field UV coverage will detect SCE within hours of an explosion, resolving the blue excess of the shock breakout phase that optical surveys currently miss. This will deliver high-cadence, high-quality NUV light curves for these early stages.

Using CCSN rates derived from W. Li et al. (2011) of (7.05 1.56) $\times$ 10^{-5} SN Mpc^{-3} yr^{-1} and assuming that SNe IIb constitute 10.6% of CCSNe (N. Smith et al. 2011), the estimate for the local SN IIb rate is approximately 0.747 $\times$ 10^{-5} SN Mpc^{-3} yr^{-1}. Assuming an initial peak of $M_{\rm NUV}$ -17 for SNe IIb, ULTRASAT's 200 deg^2 field of view and 22.5 mag sensitivity (Y. Shvartzvald et al. 2024) yield a detection rate of 77–100 SN IIb per year, for a detection horizon up to 800 Mpc. However, for an SN 2024uwq−analogous SN IIb, only those within $\lesssim$200 Mpc will have well-sampled light curves ($\leqslant$20 days) to fully characterize the shock cooling phase, as shown in Figure 12. This reduced detection horizon, the intrinsic diversity in initial SESN peak UV luminosities ($M_{\rm NUV}$ -16 to -18), and extinction considerations, combined with SN IIb volumetric rates and ULTRASAT's field of view, suggest that only approximately two to three SN IIb events per year will be observed for detailed progenitor studies. UVEX will complement ULTRASAT by providing synoptic UV spectroscopy, critical for disentangling line-forming regions in early phases, while LSST's deep optical cadence, though less frequent in the UV, will deliver statistically robust populations to contextualize binary fractions and explosion asymmetries.

8. Conclusions

We have presented early high-cadence multiwavelength photometric and spectroscopic observations of SN 2024uwq, an SN IIb with characteristic SCE. Our main conclusions are summarized below.

1. The early light curve of SN 2024uwq exhibits a double-peaked profile, with an initial maximum of M_B = -16.3 mag at t 2 days, followed by a brighter second peak at $M_B = -17.5$ mag at t 20 days. The shock cooling phase lasts 5 days, suggesting a partially stripped progenitor.
2. The early-phase spectra display broad H and He I P Cygni profiles with initial velocities of 15,500 km s^{-1} and 14,000 km s^{-1} that decline to 10,000 km s^{-1} and 7000 km s^{-1} by t 30 days, reflecting a hydrogen envelope overlying the He-rich ejecta.
3. The Arnett model fits yield ejecta and nickel parameters of $M_{\rm ej} = 3.00^{+0.10}_{-0.09}\,M_\odot$, E_k = 2.75 $\times$ 10^{51} erg, and $M_{^{56}\rm Ni}$ = 0.098 $M_\odot$, which are consistent with typical Type IIb SESNe.
4. Shock cooling models constrain the progenitor's radius to R = 14.6–57.1 $R_\odot$ and the hydrogen envelope mass to M_e = 0.7–1.35 $M_\odot$. The inferred shock velocities (v_s (0.5–2.0) $\times$ 10^4 km s^{-1}) agree with observed expansion velocities for SN 2024uwq.
5. The progenitor was likely a 12–20 $M_\odot$ ZAMS star that evolved to become a BSG/YSG likely in a binary system, positioning SN 2024uwq within the observed continuum of SNe IIb, ranging from highly stripped events (e.g., SN 2008ax, SN 2011ei) to minimally stripped ones (e.g., SN 1993J, SN 2017jgh).

The synergy of ULTRASAT's wide-field sky coverage, UVEX's spectroscopic characterization, and LSST's comprehensive volumetric surveys promises to disentangle current model degeneracies in SESN progenitor scenarios and mass-loss mechanisms. This integrated approach will move beyond the study of individual transients like SN 2024uwq, enabling population-level analyses of rich multiwavelength data sets that will provide critical insights into the evolutionary pathways of massive stars.

Acknowledgments

We thank the referee for suggestions that have improved the content and presentation of this Letter. We thank Yossi Shvartzvald for generously providing the total throughput, limiting magnitude, and source data for ULTRASAT, used in

this work. Time-domain research by the University of Arizona team and D.J.S. is supported by National Science Foundation (NSF) grants 2108032, 2308181, 2407566, and 2432036 and the Heising-Simons Foundation under grant No. 2020-1864. This work makes use of data from the Las Cumbres Observatory global telescope network, which is supported by NSF grants AST-1911225 and AST-1911151. S.V. and the UC Davis time-domain research team acknowledge support by NSF grants AST-2407565. J.E.A. and T.R.G are supported by the international Gemini Observatory, a program of NSF's NOIRLab, which is managed by the Association of Universities for Research in Astronomy (AURA) under a cooperative agreement with the National Science Foundation, on behalf of the Gemini partnership of Argentina, Brazil, Canada, Chile, the Republic of Korea, and the United States of America. K.A.B. is supported by an LSST-DA Catalyst Fellowship; this publication was thus made possible through the support of grant 62192 from the John Templeton Foundation to LSST-DA. S.H.P. and S.-C.Y. are supported by the National Research Foundation of Korea (NRF RS-2024-00356267).

The SALT spectra presented here were obtained through the Rutgers University SALT programs 2023-1-MLT-008, 2023-2-SCI-030, and 2024-1-MLT-003 (PI: Jha). Observations for this work were also obtained at the Southern Astrophysical Research (SOAR) telescope, which is a joint project of the Ministério da Ciência, Tecnologia e Inovações (MCTI/LNA) do Brasil, the US National Science Foundation's NOIRLab, the University of North Carolina at Chapel Hill (UNC), and Michigan State University (MSU). We acknowledge the important contribution of David Sanmartim, who developed the initial incarnation of the redccd module. The authors thank Tina Armond for her invaluable help in adding calibrated comparison lamps to the library of reference comparison lamps for wavelength solution. Our work would not be possible without the friendly work atmosphere at CTIO headquarters in La Serena, where we can interact with our SOAR and CTIO colleagues in lively and useful discussions that have been important in making the Goodman pipeline possible. We also acknowledge fruitful discussions and suggestions from our colleagues Bart Dunlop, Chris Clemens, and Erik Dennihy at the University of North Carolina at Chapel Hill.

This work has made use of data from the Asteroid Terrestrial-impact Last Alert System (ATLAS) project. The Asteroid Terrestrial-impact Last Alert System (ATLAS) project is primarily funded to search for near-Earth asteroids through NASA grants NN12AR55G, 80NSSC18K0284, and 80NSSC18K1575; by-products of the NEO search include images and catalogs from the survey area. This work was partially funded by the Kepler/K2 grant J1944/80NSSC19K0112, HST GO-15889, and the STFC grants ST/T000198/1 and ST/S006109/1. The ATLAS science products were made possible through the contributions of the University of Hawaii Institute for Astronomy, Queen's University Belfast, the Space Telescope Science Institute, the South African Astronomical Observatory, and the Millennium Institute of Astrophysics (MAS), Chile. This research has made use of the NASA Astrophysics Data System (ADS) Bibliographic Services and the NASA/IPAC Infrared Science Archive (IRSA), which is funded by the National Aeronautics and Space Administration and operated by the California Institute of Technology. This work also made use of data supplied by the UK Swift Science Data Centre at the University of Leicester.

Facilities: ADS, Swift (UVOT), AAVSO, NED, LCOGT (Sinistro, FLOYDS), SOAR (Goodman), SALT (RSS), ATLAS.

*S*oftware: Astropy (Astropy Collaboration et al. 2013; A. M. Price-Whelan et al. 2018; Astropy Collaboration et al. 2022), Photutils (L. Bradley et al. 2022), BANZAI (C. McCully et al. 2018), Light Curve Fitting (G. Hosseinzadeh et al. 2024), `emcee` (D. Foreman-Mackey et al. 2013), `corner` (D. Foreman-Mackey 2016), `Superbol` (M. Nicholl 2018), `shock cooling-curve` (P. Venkatraman & W. Jacobson-Galán 2024), Matplotlib (J. D. Hunter 2007), Numpy (C. R. Harris et al. 2020), Scipy (P. Virtanen et al. 2020), IRAF (D. Tody 1986, 1993), PySALT (S. M. Crawford et al. 2010), Goodman-HTS pipeline (S. Torres-Robledo et al. 2020), FLOYDS pipeline (S. Valenti et al. 2014), `lcogtsnpipe`(S. Valenti et al. 2016).

Appendix

Table 3 provides the log of spectroscopic observations, including dates, instruments, phases, and exposure times used in this study.

Table 3
Log of Spectroscopic Observations

Date (UTC)	MJD	Telescope	Instrument	Phase (days)	Exp (s)
2024-09-09 13:06:50	60562.54	COJ[a]	FLOYDS	3.91	1800
2024-09-09 22:50:20	60562.95	SALT	RSS	4.31	1133
2024-09-10 10:02:18	60563.41	COJ	FLOYDS	4.78	1800
2024-09-13 11:58:50	60566.49	COJ	FLOYDS	7.86	1800
2024-09-15 13:24:33	60568.55	COJ	FLOYDS	9.92	1800
2024-09-16 21:59:53	60569.91	SALT	RSS	11.28	1500
2024-09-18 10:39:17	60571.44	COJ	FLOYDS	12.81	1800
2024-09-22 11:28:15	60575.47	COJ	FLOYDS	16.84	1800
2024-09-28 02:05:25	60581.08	SOAR	GHTS-Red	22.45	400
2024-09-28 10:18:09	60581.42	COJ	FLOYDS	22.79	1800
2024-10-01 10:19:49	60584.43	COJ	FLOYDS	25.79	1800
2024-10-03 21:08:56	60586.88	SALT	RSS	28.2	1500
2024-10-05 03:48:50	60588.15	SOAR	GHTS-Red	29.52	400
2024-10-07 20:37:40	60590.85	SALT	RSS	32.22	1500
2024-10-10 12:12:34	60593.50	COJ	FLOYDS	34.87	1800
2024-10-17 19:57:33	60600.83	SALT	RSS	42.19	1500
2024-10-19 15:58:16	60602.66	SALT	RSS	44.03	1500
2024-10-20 11:35:34	60603.48	COJ	FLOYDS	44.84	1800
2024-10-22 02:57:21	60605.12	SOAR	GHTS-Red	46.48	400
2024-10-25 11:29:18	60608.47	COJ	FLOYDS	49.84	1800
2024-10-29 11:08:12	60612.46	COJ	FLOYDS	53.83	1800
2024-11-03 10:12:11	60617.42	COJ	FLOYDS	58.79	1800
2024-11-08 10:35:24	60622.44	COJ	FLOYDS	63.80	1800
2024-11-18 10:35:24	60632.50	Gemini-S	FLAMINGOS-2	76.40	1800

Note.
[a] COJ is the site code for the Siding Spring Observatory, Australia, which hosts 1 and 2 m class telescopes as a part of the Las Cumbres Observatory network.

ORCID iDs

Bhagya M. Subrayan https://orcid.org/0000-0001-8073-8731
David J. Sand https://orcid.org/0000-0003-4102-380X
K. Azalee Bostroem https://orcid.org/0000-0002-4924-444X
Saurabh W. Jha https://orcid.org/0000-0001-8738-6011
Aravind P. Ravi https://orcid.org/0000-0002-7352-7845
Michaela Schwab https://orcid.org/0009-0002-5096-1689
Jennifer E. Andrews https://orcid.org/0000-0003-0123-0062
Griffin Hosseinzadeh https://orcid.org/0000-0002-0832-2974
Stefano Valenti https://orcid.org/0000-0001-8818-0795
Yize Dong (董一泽) https://orcid.org/0000-0002-7937-6371
Jeniveve Pearson https://orcid.org/0000-0002-0744-0047
Manisha Shrestha https://orcid.org/0000-0002-4022-1874
Lindsey A. Kwok https://orcid.org/0000-0003-3108-1328
Emily Hoang https://orcid.org/0000-0003-2744-4755
Jeonghee Rho https://orcid.org/0000-0003-3643-839X
Seong Hyun Park https://orcid.org/0000-0001-7488-4337
Sung-Chul Yoon https://orcid.org/0000-0002-5847-8096
T. R. Geballe https://orcid.org/0000-0003-2824-3875
Joshua Haislip https://orcid.org/0000-0002-6703-805X
Daryl Janzen https://orcid.org/0000-0003-0549-3281
Vladimir Kouprianov https://orcid.org/0000-0003-3642-5484
Darshana Mehta https://orcid.org/0009-0008-9693-4348
Nicolás Meza Retamal https://orcid.org/0000-0002-7015-3446
Daniel E. Reichart https://orcid.org/0000-0002-5060-3673
Moira Andrews https://orcid.org/0000-0002-1895-6639
Joseph Farah https://orcid.org/0000-0003-4914-5625
Megan Newsome https://orcid.org/0000-0001-9570-0584
D. Andrew Howell https://orcid.org/0000-0003-4253-656X
Curtis McCully https://orcid.org/0000-0001-5807-7893

References

Aldering, G., Humphreys, R. M., & Richmond, M. 1994, AJ, 107, 662
Andrews, J. E., Pearson, J., Hosseinzadeh, G., et al. 2024, ApJ, 965, 85
Arcavi, I., Gal-Yam, A., Yaron, O., et al. 2011, ApJL, 742, L18
Arcavi, I., Hosseinzadeh, G., Brown, P. J., et al. 2017, ApJL, 837, L2
Armstrong, P., Tucker, B. E., Rest, A., et al. 2021, MNRAS, 507, 3125
Arnett, W. D. 1982, ApJ, 253, 785
Astropy Collaboration, Price-Whelan, A. M., Lim, P. L., et al. 2022, ApJ, 935, 167
Astropy Collaboration, Robitaille, T. P., Tollerud, E. J., et al. 2013, A&A, 558, A33
Barbon, R., Benetti, S., Cappellaro, E., et al. 1995, A&AS, 110, 513
Bersten, M. C., Benvenuto, O. G., Nomoto, K., et al. 2012, ApJ, 757, 31
Bersten, M. C., Folatelli, G., García, F., et al. 2018, Natur, 554, 497
Blondin, S., & Tonry, J. L., 2011 SNID: Supernova Identification, Astrophysics Source Code Library, ascl:1107.001
Bostroem, K. A. 2024, TNSCR, 2024-3548, 1
Bradley, L., Sipőcz, B., Robitaille, T., et al. 2022, astropy/photutils: v1.6.0, Zenodo, doi:10.5281/zenodo.7419741
Breeveld, A. A., Curran, P. A., Hoversten, E. A., et al. 2010, MNRAS, 406, 1687
Brown, T. M., Baliber, N., Bianco, F. B., et al. 2013, PASP, 125, 1031
Bufano, F., Pignata, G., Bersten, M., et al. 2014, MNRAS, 439, 1807
Cardelli, J. A., Clayton, G. C., & Mathis, J. S. 1989, ApJ, 345, 245
Chatzopoulos, E., Wheeler, J. C., & Vinko, J. 2012, ApJ, 746, 121
Chevalier, R. A., & Fransson, C. 1994, ApJ, 420, 268
Chevalier, R. A., & Soderberg, A. M. 2010, ApJL, 711, L40
Chornock, R., Filippenko, A. V., Li, W., et al. 2011, ApJ, 739, 41
Claeys, J. S. W., de Mink, S. E., Pols, O. R., Eldridge, J. J., & Baes, M. 2011, A&A, 528, A131
Crawford, S. M., Still, M., Schellart, P., et al. 2010, Proc. SPIE, 7737, 773725
Crockett, R. M., Eldridge, J. J., Smartt, S. J., et al. 2008, MNRAS, 391, L5
Das, K. K., Kasliwal, M. M., Fremling, C., et al. 2023, ApJ, 959, 12
Dessart, L., Hillier, D. J., Waldman, R., & Livne, E. 2013, MNRAS, 433, 1745
Dong, Y., Valenti, S., Ashall, C., et al. 2024, ApJ, 974, 316
Eikenberry, S., Bandyopadhyay, R., Bennett, J. G., et al. 2012, Proc. SPIE, 8446, 84460I

Eikenberry, S. S., Elston, R., Raines, S. N., et al. 2004, Proc. SPIE, 5492, 1196
Ergon, M., Jerkstrand, A., Sollerman, J., et al. 2015, A&A, 580, A142
Ergon, M., Sollerman, J., Fraser, M., et al. 2014, A&A, 562, A17
Farah, J. R., Howell, D. A., Terreran, G., et al. 2025, ApJ, 984, 60
Filippenko, A. V. 1988, AJ, 96, 1941
Filippenko, A. V. 1997, ARA&A, 35, 309
Filippenko, A. V., Matheson, T., & Ho, L. C. 1993, ApJL, 415, L103
Foreman-Mackey, D. 2016, JOSS, 1, 24
Foreman-Mackey, D., Hogg, D. W., Lang, D., & Goodman, J. 2013, PASP, 125, 306
Gal-Yam, A. 2017, in Handbook of Supernovae, ed. A. W. Alsabti & P. Murdin (Berlin: Springer), 195
Gehrels, N., Chincarini, G., Giommi, P., et al. 2004, ApJ, 611, 1005
Georgy, C., Ekström, S., Saio, H., et al. 2013, in EAS Publications Series, ed. P. Kervella, T. Le Bertre, & G. Perrin, Vol. 60 (Les Ulis: EDP Sciences), 43
Goldberg, J. A., Jiang, Y.-F., Bildsten, L., et al. 2022, ApJ, 933, 164
González-Bañuelos, M., Gutiérrez, C. P., Galbany, L., & González-Gaitán, S. 2025, arXiv:2507.08731
Groh, J., Meynet, G., Ekstrom, S., & Georgy, C. 2013a, GRBs and Their Hosts as Tracers of the High Redshift Universe (Les Ulis: EDP Sciences), 16
Groh, J. H., Meynet, G. A., Ekström, G., et al. 2013b, in EAS Publications Series, ed. P. Kervella, T. Le Bertre, & G. Perrin, Vol. 60 (Les Ulis: EDP Sciences), 51
Hakobyan, A. A., Mamon, G. A., Petrosian, A. R., Kunth, D., & Turatto, M. 2009, A&A, 508, 1259
Harris, C. R., Millman, K. J., van der Walt, S. J., et al. 2020, Natur, 585, 357
Harutyunyan, A. H., Pfahler, P., Pastorello, A., et al. 2008, A&A, 488, 383
Haynie, A., & Piro, A. L. 2023, ApJ, 956, 98
Henden, A. A., Welch, D. L., Terrell, D., & Levine, S. E. 2009, AAS Meeting, 214, 407.02
Hosseinzadeh, G., Bostroem, K. A., Ben-Ami, T., & Gomez, S. 2024, Light Curve Fitting v0.10.0, Zenodo, doi:10.5281/zenodo.11405219
Hosseinzadeh, G., Farah, J., Shrestha, M., et al. 2023, ApJL, 953, L16
Howell, A. 2024, AAS Meeting, 243, 232.01
Hunter, J. D. 2007, CSE, 9, 90
Irani, I., Morag, J., Gal-Yam, A., et al. 2024, ApJ, 970, 96
Ivezić, Ž., Kahn, S. M., Tyson, J. A., et al. 2019, ApJ, 873, 111
Jerkstrand, A., Fransson, C., Maguire, K., et al. 2012, A&A, 546, A28
Jordi, K., Grebel, E. K., & Ammon, K. 2006, A&A, 460, 339
Kasen, D., & Bildsten, L. 2010, ApJ, 717, 245
Katz, B., Sapir, N., & Waxman, E. 2012, ApJ, 747, 147
Kelly, P. L., & Kirshner, R. P. 2012, ApJ, 759, 107
Kilpatrick, C. D., Coulter, D. A., Foley, R. J., et al. 2022, ApJ, 936, 111
Kulkarni, S. R., Harrison, F. A., Grefenstette, B. W., et al. 2021, arXiv:2111.15608
Landolt, A. U. 1992, AJ, 104, 340
Laplace, E., Justham, S., Renzo, M., et al. 2021, A&A, 656, A58
Li, W., Chornock, R., Leaman, J., et al. 2011, MNRAS, 412, 1473
Long, G., Song, H., Meynet, G., et al. 2022, ApJS, 262, 26
Lyman, J. D., Bersier, D., James, P. A., et al. 2016, MNRAS, 457, 328
Matheson, T., Filippenko, A. V., Ho, L. C., Barth, A. J., & Leonard, D. C. 2000, AJ, 120, 1499
Matzner, C. D., & McKee, C. F. 1999, ApJ, 510, 379
Maund, J. R., Fraser, M., Ergon, M., et al. 2011, ApJL, 739, L37
McCully, C., Volgenau, N. H., Harbeck, D.-R., et al. 2018, Proc. SPIE, 10707, 107070K
Meza-Retamal, N., Dong, Y., Bostroem, K. A., et al. 2024, ApJ, 971, 141
Milisavljevic, D., Margutti, R., Soderberg, A. M., et al. 2013, ApJ, 767, 71
Modjaz, M., Blondin, S., Kirshner, R. P., et al. 2014, AJ, 147, 99
Morag, J., Sapir, N., & Waxman, E. 2023, MNRAS, 522, 2764
Morales-Garoffolo, A., Elias-Rosa, N., Benetti, S., et al. 2014, MNRAS, 445, 1647
Morales-Garoffolo, A., Elias-Rosa, N., Bersten, M., et al. 2015, MNRAS, 454, 95
Moriya, T. J., Subrayan, B. M., Milisavljevic, D., & Blinnikov, S. I. 2023, PASJ, 75, 634
Nakar, E., & Piro, A. L. 2014, ApJ, 788, 193
Nakar, E., & Sari, R. 2010, ApJ, 725, 904
Nicholl, M. 2018, RNAAS, 2, 230
Ouchi, R., & Maeda, K. 2017, ApJ, 840, 90
Pastorello, A., Kasliwal, M. M., Crockett, R. M., et al. 2008, MNRAS, 389, 955
Pellegrino, C., Hiramatsu, D., Arcavi, I., et al. 2023, ApJ, 954, 35
Piro, A. L. 2015, ApJL, 808, L51
Piro, A. L., Haynie, A., & Yao, Y. 2021, ApJ, 909, 209
Podsiadlowski, P. 2008, in ASP Conf. Ser. 391, Hydrogen-Deficient Stars, ed. A. Werner & T. Rauch (San Francisco, CA: ASP), 323
Poznanski, D., Prochaska, J. X., & Bloom, J. S. 2012, MNRAS, 426, 1465
Price-Whelan, A. M., Sipőcz, B. M., Günther, H. M., et al. 2018, AJ, 156, 123
Rabinak, I., & Waxman, E. 2011, ApJ, 728, 63
Ramirez, M., Ayala, B., Dastidar, R., Kumar, A., & Yaron, O. 2024, TNSCR, 2024-3408, 1
Reguitti, A., Pastorello, A., Smartt, S. J., et al. 2025, arXiv:2503.03851
Reichart, D., Nysewander, M., Moran, J., et al. 2005, NCimC, 28, 767
Rho, J., Geballe, T. R., Banerjee, D. P. K., et al. 2018, ApJL, 864, L20
Richmond, M. W., Treffers, R. R., Filippenko, A. V., et al. 1994, AJ, 107, 1022
Rizzo Smith, M., Kochanek, C. S., & Neustadt, J. M. M. 2023, MNRAS, 523, 1474
Roming, P. W. A., Kennedy, T. E., Mason, K. O., et al. 2005, SSRv, 120, 95
Sapir, N., Katz, B., & Waxman, E. 2011, ApJ, 742, 36
Sapir, N., Katz, B., & Waxman, E. 2013, ApJ, 774, 79
Sapir, N., & Waxman, E. 2017, ApJ, 838, 130
Schlafly, E. F., & Finkbeiner, D. P. 2011, ApJ, 737, 103
Shahbandeh, M., Hsiao, E. Y., Ashall, C., et al. 2022, ApJ, 925, 175
Shivvers, I., Filippenko, A. V., Silverman, J. M., et al. 2019, MNRAS, 482, 1545
Shrestha, M., Bostroem, K. A., Sand, D. J., et al. 2024a, ApJL, 972, L15
Shrestha, M., Pearson, J., Wyatt, S., et al. 2024b, ApJ, 961, 247
Shussman, T., Waldman, R., & Nakar, E. 2016, arXiv:1610.05323
Shvartzvald, Y., Waxman, E., Gal-Yam, A., et al. 2024, ApJ, 964, 74
Smartt, S. J. 2015, PASA, 32, e016
Smith, K. W., Nordsieck, K. H., Burgh, E. B., et al. 2006, Proc. SPIE, 6269, 62692A
Smith, K. W., Smartt, S. J., Young, D. R., et al. 2020, PASP, 132, 085002
Smith, N. 2014, ARA&A, 52, 487
Smith, N., Li, W., Filippenko, A. V., & Chornock, R. 2011, MNRAS, 412, 1522
Soderberg, A. M., Margutti, R., Zauderer, B. A., et al. 2012, ApJ, 752, 78
Soker, N. 2017, arXiv:1709.01388
Sravan, N., Marchant, P., Kalogera, V., Milisavljevic, D., & Margutti, R. 2020, ApJ, 903, 70
Sukhbold, T., Ertl, T., Woosley, S. E., Brown, J. M., & Janka, H. T. 2016, ApJ, 821, 38
Sukhbold, T., Woosley, S. E., & Heger, A. 2018, ApJ, 860, 93
Taddia, F., Stritzinger, M. D., Bersten, M., et al. 2018, A&A, 609, A136
Tartaglia, L., Fraser, M., Sand, D. J., et al. 2017, ApJL, 836, L12
Tartaglia, L., Sand, D. J., Valenti, S., et al. 2018, ApJ, 853, 62
Taubenberger, S., Navasardyan, H., Maurer, J. I., et al. 2011, MNRAS, 413, 2140
Tody, D. 1986, Proc. SPIE, 627, 733
Tody, D. 1993, in ASP Conf. Ser. 52, Astronomical Data Analysis Software and Systems II, ed. R. J. Hanisch, R. J. V. Brissenden, & J. Barnes (San Francisco, CA: ASP), 173
Tonry, J., Denneau, L., Weiland, H., et al. 2024, TNSTR, 2024-3352, 1
Tonry, J. L., Denneau, L., Heinze, A. N., et al. 2018, PASP, 130, 064505
Torres-Robledo, S., Briceño, C., Quint, B., & Sanmartim, D. 2020, in ASP Conf. Ser. 522, Astronomical Data Analysis Software and Systems XXVII, ed. P. Ballester et al. (San Francisco, CA: ASP), 533
Tully, R. B., Rizzi, L., Shaya, E. J., et al. 2009, AJ, 138, 323
Valenti, S., Benetti, S., Cappellaro, E., et al. 2008, MNRAS, 383, 1485
Valenti, S., Howell, D. A., Stritzinger, M. D., et al. 2016, MNRAS, 459, 3939
Valenti, S., Sand, D., Pastorello, A., et al. 2014, MNRAS, 438, 101
Van Dyk, S. D., Zheng, W., Fox, O. D., et al. 2014, AJ, 147, 37
Vartanyan, D., Laplace, E., Renzo, M., et al. 2021, ApJL, 916, L5
Venkatraman, P., & Jacobson-Galán, W. 2024, RNAAS, 8, 33
Vink, J. S., Muijres, L. E., Anthonisse, B., et al. 2011, A&A, 531, A132
Virtanen, P., Gommers, R., Oliphant, T. E., et al. 2020, NatMe, 17, 261
Woosley, S. E. 2010, ApJL, 719, L204
Woosley, S. E., Eastman, R. G., Weaver, T. A., & Pinto, P. A. 1994, ApJ, 429, 300
Woosley, S. E., Langer, N., & Weaver, T. A. 1993, ApJ, 411, 823
Yaron, O., & Gal-Yam, A. 2012, PASP, 124, 668
Yoon, S.-C., Dessart, L., & Clocchiatti, A. 2017, ApJ, 840, 10